Nano Energy 100 (2022) 107478

Contents lists available at ScienceDirect

Nano Energy

journal homepage: www.elsevier.com/locate/nanoen

Realizing high thermoelectric performance in eco-friendly Bi_2S_3 with nanopores and Cl-doping through shape-controlled nano precursors

Kangpeng Jin [a], Janak Tiwari [b], Tianli Feng [b,*], Yue Lou [a,*], Biao Xu [a,*]

[a] School of Chemistry and Chemical Engineering, Nanjing University of Science and Technology, Nanjing 210094, China
[b] Department of Mechanical Engineering, The University of Utah, Salt Lake City, UT 84112, USA

ARTICLE INFO

Keywords:
Thermoelectric
Bi_2S_3
Nanopores
Four-phonon scattering
DFT calculation

ABSTRACT

Porous materials have attracted extensive attention from research communities, showing great promise in energy-conversion applications. In this study, we prepared eco-friendly Bi_2S_3-based thermoelectric materials with porous structure using reticulated Bi_2S_3 nanonetwork synthesized by a solution-phase bottom-up strategy. Comprehensive structural characterizations through small-angle X-ray scattering (SAXS) and electron microscopy were performed to measure the pore structures in these materials. The distorted lattices, dense dislocations, and nanopores reduce the material's lattice thermal conductivity to as low as 0.36 $Wm^{-1}K^{-1}$ at 823 K, which is 22% lower than that of the less porous counterpart. Simultaneously, Cl was doped into the lattice, which greatly improved the electrical conductivity and mitigated the deterioration of the electrical performance by the pore structure. The maximum power factor reaches 0.47 $mWm^{-1}K^{-2}$. The synergistic effect of nanopores and Cl doping greatly improves the thermoelectric properties of the Bi_2S_3 system, and the highest ZT value reaches 0.81 at 823 K, which is nearly 60% higher than that of the control sample with fewer pores. This work develops a new strategy for the preparation of high-performance and light-weight thermoelectric materials.

1. Introduction

With excellent performance in transforming heat to electricity directly, thermoelectric materials (TE) have attracted much attention [1,2]. Usually, the conversion efficiency of TE materials is gauged by a dimensionless figure of merit, $ZT = S^2\sigma T/\kappa$ in which S is Seebeck coefficient, σ is electrical conductivity and κ is thermal conductivity. $S^2\sigma$ is usually defined as the power factor, reflecting the material's output power of thermoelectric conversion. The κ can be divided into lattice thermal conductivity κ_L and electronic thermal conductivity κ_e, which are attributed to lattice vibration and electron gas, respectively. In order to optimize the thermoelectric performance, it is necessary to decouple the S, σ, and κ to improve the power factor and reduce the thermal conductivity.

Bi_2S_3 is a low-toxicity semiconductor material with an indirect bandgap of 1.3–1.7 eV [3–5], which has intrigued the research communities due to its advantages such as earth-abundant constituent elements, intrinsic low thermal conductivity, and good processability. After years, researchers have exhausted multiple means to optimize the ZT of Bi_2S_3 families. In the electrical aspect, strategies such as doping n-type elements to adjust the carrier concentration [6,7], doping rare earth elements to introduce impurity levels [8,9], and constructing a core-shell structure to filter low energy carriers [10–12] are used to improve the power factor. In the thermal aspect, most studies focused on the fabrication of multiscale defects to scatter phonons with different wavelengths, such as alloying, high density of grain boundaries [13,14], dislocations [15], and nano-precipitates [16,17].

In recent years, porous materials have attracted extensive attention in catalysis [18–21], battery [22–24], sensor [25,26], and other fields due to their high specific surface area, multiple active sites, and mesoscale cavity structure, while porous thermoelectric materials have rarely been reported [27]. The lattice thermal conductivity can be expressed as $\kappa_L = \frac{1}{3}C_v v_g \Lambda$, in which C_v, v_g, and Λ represent heat capacity at constant volume, phonon group velocity, and phonon mean free path, respectively. Compared with the dense material, the porous counterpart can significantly reduce heat capacity and sound velocity, and the impact on thermal conductivity is explained by effective medium theory [28,29]. When the pore size is close to the mean free path (Λ), it can also scatter phonons, resulting in even lower thermal conductivity [30,31]. Thus, constructing a porous structure with controllable pore size is a sufficient way to reduce κ_L. Meanwhile, reducing the mass density of

* Corresponding authors.
E-mail addresses: tianli.feng@utah.edu (T. Feng), louyue@njust.edu.cn (Y. Lou), xubiao@njust.edu.cn (B. Xu).

https://doi.org/10.1016/j.nanoen.2022.107478
Received 26 October 2021; Received in revised form 17 May 2022; Accepted 6 June 2022
Available online 9 June 2022

thermoelectric materials by pores plays a significant role in improving the portability of devices but remains largely unexplored.

For the synthesis of porous materials, the commonly used top-down synthetic methods such as melting or mechanical alloying do not work well since the size and morphology of powder precursors cannot be finely controlled. Inevitably, the sintered monoliths usually have high density and non-porous structures [6,9]. By contrast, bottom-up solution-processed production is a potentially efficient alternative to conventional methods. But in this scenario, a high degree of control over the relative density of the final bulk matrix after sintering still represents a grand challenge because 2D nanosheets/ 1D nanotubes/ 0D nanodots tend to be tightly tiled under pressure. In an effort to make good use of the reduction of lattice thermal conductivity by the pore structure in monoliths, synthesizing sized-controlled nanocrystals with porous morphologies such as hollow, concave, and branched nanostructures as precursors are proved to be efficient [30]. From a synthetic perspective, creating a framework structure derived from a two-dimensional self--assembly structure can be an effective tool to solve this problem.

In this work, we have successfully prepared two kinds of powder samples via solution methods: nano network (NN) and randomly oriented nanorods (NR). They can be prepared by either hydrothermal autoclaves (HT) or glass flasks (FL). The shape-controlled network-like sample is used as a precursor to construct the porous thermoelectric materials, as illustrated in Fig. 1a. Small-angle X-ray scattering (SAXS) and electron microscopy are applied to study the pore structure, as shown in Fig. 1b. With a large amount of properly sized nanopores as well as abundant grain boundaries, its thermal conductivity can be reduced to a significantly low value. We also note that four-phonon scattering is important in Bi_2S_3, as has been found in other thermoelectric materials very recently [32–35]. Our first-principles simulations further support that. On the electrical aspect, Cl is successfully doped into the lattice, compensating for the deterioration in electron mobility caused by the porous structure. First-principles calculation shows that the introduction of Cl brings the Fermi level into conduction bands, and the carrier concentration is greatly increased (Fig. 1c). As a result, both NN and NR samples have excellent electrical properties compared with those of pristine Bi_2S_3 reported in other literature [6,7,36]. A peak *ZT* of 0.81 at 823 K is obtained for the monolith sintered by the more porous sample (HT-NN), which is 60% higher than the less porous counterpart (HT-NR) and among the best Bi_2S_3 thermoelectric materials (Fig. 1d).

2. Experimental section

2.1. Reagents

Bismuth chloride ($BiCl_3$, A.R., 99%) was purchased from Energy-Chemical Co., Ltd. Thioacetamide (TAA, A.R., 99%) was purchased from Shanghai Macklin Biochemical Technology Co., Ltd. Hydrochloric acid (HCl, A.R, 36%) was purchased from Sinopharm Chemical Reagent Co., Ltd. Ultra-pure water was used as solvent with a resistivity of 18.25 MΩ·cm.

2.2. Preparation of nanostructure precursors and bulk samples with porous structure

Bi_2S_3 network nanodiscs (HT-NN) were synthesized through the hydrothermal method. In a typical process, 2.5 mL of $BiCl_3$ (1 mmol) and HCl (5 mmol) solution was added to 42.5 mL H_2O. Then white BiOCl precipitate was formed. 15 mL of TAA (10 mmol) solution was added in drops with magnetic agitation. When the suspension changed color from white to brown, the mixture was transferred to a Teflon-lined stainless-steel autoclave (100 mL) and reacted at 180 ℃ for 3 h. Black Bi_2S_3 precipitate was washed with DI water and ethanol 3 times, separately. The precipitated slurry was finally dried in a vacuum at 60 ℃, and the black Bi_2S_3 powder was obtained.

The randomly oriented nanorod (HT-NR) was synthesized using the same process, except with the doubled concentration of $BiCl_3$ (2 mmol).

Two kinds of powder were sintered at 823 K for 15 min using a spark plasma sinter (SPS) system (LABOX-110, Sinter Land) under an axial pressure of 20 MPa. The SPSed monoliths were cut and polished into 3 mm × 3 mm× 9 mm rectangular ingots and 10 mm × 10 mm× 1.5 mm square slice to test electrical and thermal performance in the

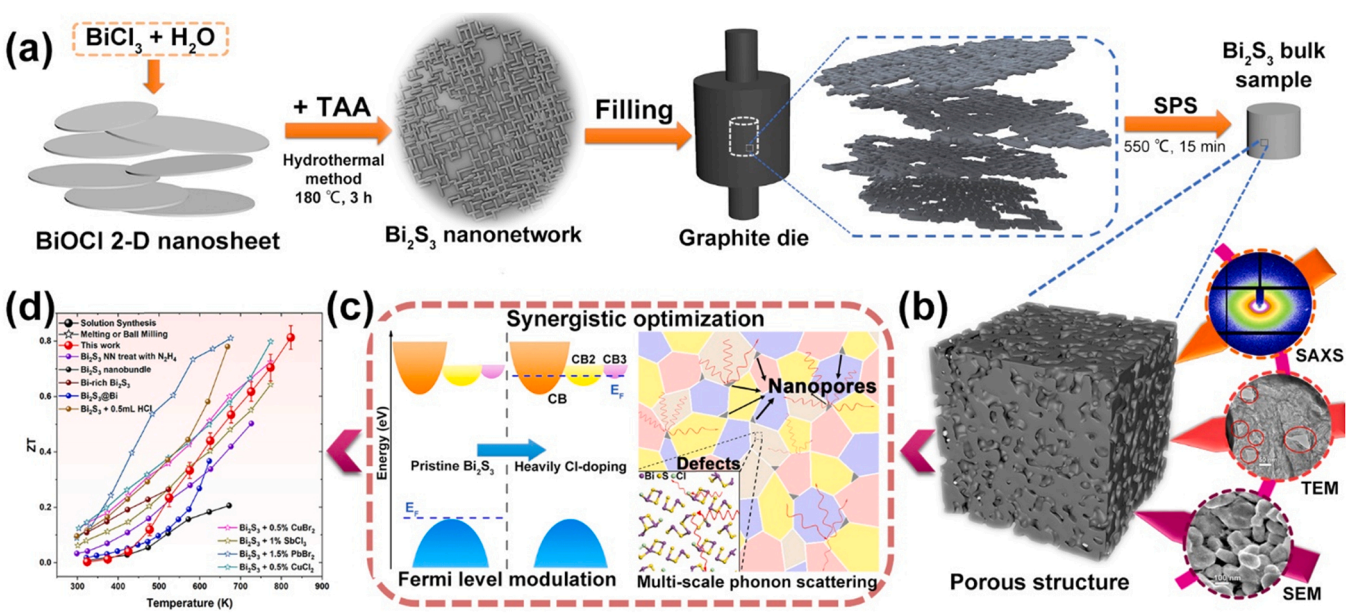

Fig. 1. (a) Illustration of experimental procedure of Bi_2S_3 bulk sample with porous structure through stacking precursor building blocks synthesized via self-template method. (b) Characterization of pores in nanoscale via small-angle X-ray scattering (SAXS), transmission electron microscopy (TEM), and scanning electron microscopy (SEM). (c) Schematic diagram of simultaneous optimization of electron and phonon transport. Fermi level rising into conduction bands increases carrier concentration. The strong 4-phonon process leads to intrinsically low κ_L. Nanopores with abundant grain boundaries and other defects further reduce the κ_L significantly. (d) A comparison between *ZT* values obtained in this work with those reported in the literature for Bi_2S_3 systems through different modification methods [6,9,12,36–41].

direction perpendicular to sintering pressure, respectively.

Since HT samples have better performance, they are discussed in detail in the main manuscript, while the characterization and TE properties of the FL samples are presented in the Supporting Information.

2.3. Measurement of thermoelectric properties

Seebeck coefficient and electrical resistivity were measured by static direct current method and four-probe method (CTA-3S, CRYALL), respectively. Thermal conductivity was calculated through the equation $\kappa = C_p \cdot \rho \cdot D$. The specific heat at constant pressure (C_p) is obtained by using a differential scanning calorimetry thermal analyzer (DSC, DSC404F3, NETZSCH). The densities of sintered specimens were measured by Archimedes method The thermal diffusivity (D) was measured by laser flash method (Discovery Xeon Flash, TA Instrument). The temperature-dependent Hall coefficients were measured by van-der-Pauw method under a reversible magnetic field of 1.5 T (Lake Shore 8400 Series). The Hall carrier concentration (n_H) and Hall mobility (μ_H) were calculated by $n_H = 1/(eR_H)$ and $\mu_H = \sigma R_H$, respectively.

The deviations of Seebeck coefficient, electrical conductivity, and thermal diffusivity are less than ± 7%, ± 10%, and ± 4%, respectively.

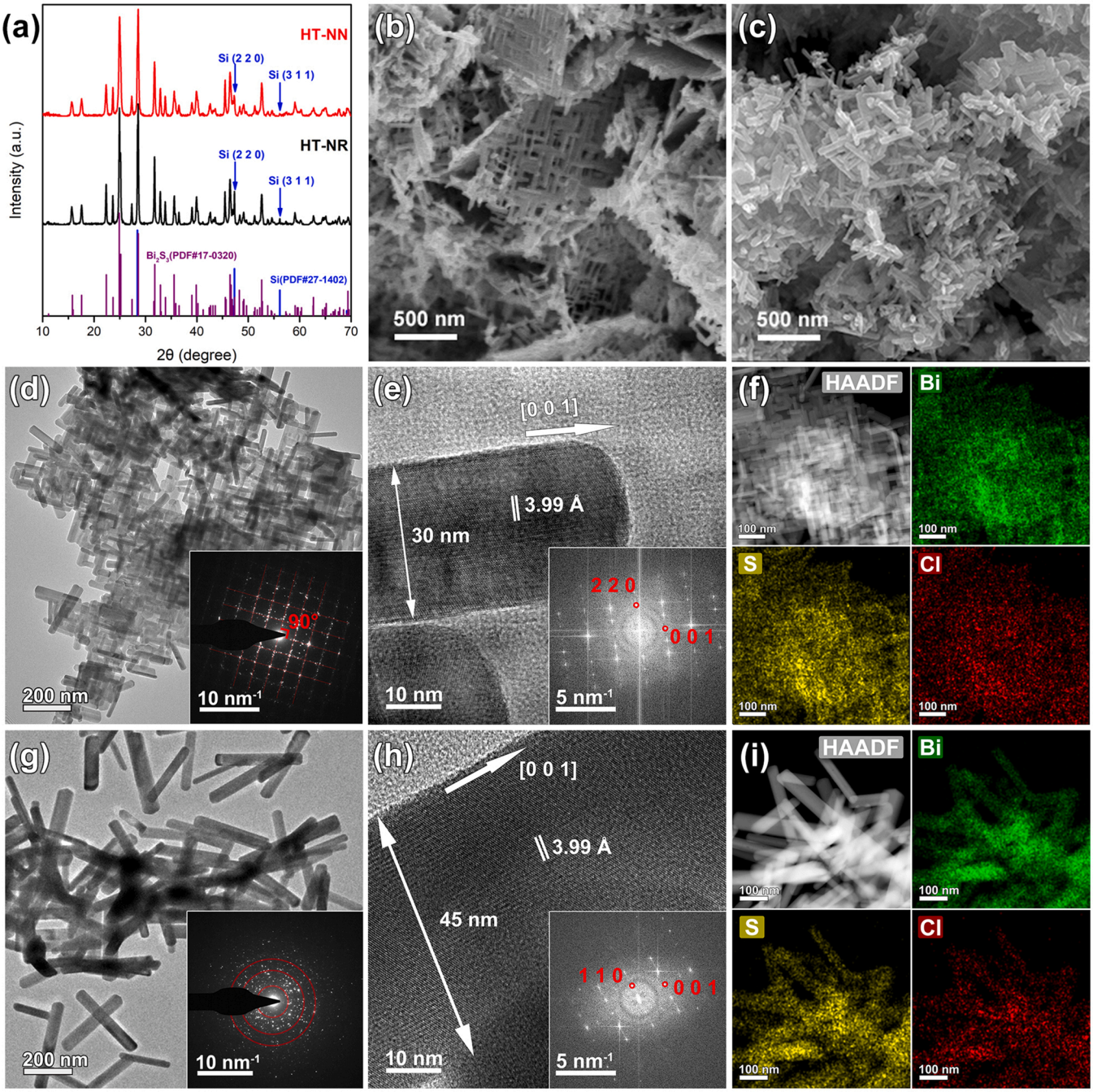

Fig. 2. Morphological and phase characterizations of as-synthesized powder precursors. (a) XRD pattern of two powder precursors; (b, c) SEM image of HT-NN and HT-NR, which shows the netted and disordered morphology; (d) low-magnification TEM image of a typical HT-NN nanodisc and its corresponding SAED pattern demonstrate the vertical growth of nanorods; (e) HR-TEM image of HT-NN single nanorod with inset of fast-Fourier transform (FFT) pattern, indicating that the nanorods grow vertically along [0 0 1] crystal axis; (g) TEM image of HT-NR with annular SAED pattern; (h) HR-TEM of HT-NR with inserted FFT image; (f, i) EDS mapping images of HT-NN and HT-NR, respectively.

3. Results and discussion

3.1. Phase and morphology of Bi_2S_3 nanopowders

Bi_2S_3 typically crystallizes in *Pnma* (62) space group. It preferentially grows along the c-axis (namely [0 0 1] axis) by the Bi-S covalent bond of the [BiS_3] trigonal pyramid unit, forming zig-zag chains. The chains are arranged in parallel and linked by van der Waals and weak ionic forces along the a-axis and b-axis. Fig. 2a shows the X-ray diffraction pattern of as-synthesized powder with different morphologies (nanonetwork and nanorods), respectively. To calibrate the location of the diffraction peaks, silicon powder was used as an inner standard. Both diffraction spectra can be indexed as pure orthorhombic Bi_2S_3 (JCPDS#17–0320). The cell parameters of these two samples are very close (Table S1).

Fig. 2b clearly shows the network structure of HT-NN, while nanorods in HT-NR (Fig. 2c) have a disordered arrangement structure and are similar in size to that of HT-NN. The morphologies of two as-synthesized powder samples are further investigated by high-resolution TEM (HR-TEM) and selected area electron diffraction (SAED), as shown in the insets of Fig. 2d and g. HT-NN consists mainly of vertically interlaced nanorods with a diameter of 45 ± 15 nm (conforming to normal distribution); HT-NR is composed of disordered nanorods with a slightly larger size than HT-NN and a single-rod diameter of 60 ± 15 nm. The SAED pattern of HT-NN is mainly composed of two sets of mutually perpendicular diffraction points that form a square matrix grid, indicating that nanorods on the disk grow almost vertically. The diffraction points slightly deviating from the grid belong to a few skewed nanorods. Moreover, the structure of orthogonally stacked nanorods can be clearly seen from the contrast information given by the HAADF image (Fig. 2f inset). The process of these topological transformations was studied in a similar reaction by Li et al. through electron diffraction [42]. With the dilution of the concentration of $BiCl_3$ hydrochloric acid solution, the 2-D precursor of BiOCl was generated by hydrolysis. As the interplanar spacing in the directions of (1 0 0) and (0 1 0) of tetragonal BiOCl was close to the dominant growth crystal plane (0 0 1) of orthorhombic Bi_2S_3. The interaction between single crystal BiOCl nanosheets and thioacetamide led to topotactic transformation, forming a disk composed of Bi_2S_3 orthogonal nanorods. In contrast, the SAED pattern of HT-NR (Fig. 2g inset) is irregularly annular, indicating that the nanorods are arranged disorderly. As Bi concentration increases in the solution, the nanorods tended to grow irregularly and the length of each nanorod became longer. According to HT-NN's HR-TEM image (Fig. 2e) and corresponding FFT pattern, the interplanar spacing is about 3.98 Å, which is consistent with the (0 0 1) crystal plane of Bi_2S_3. HT-NR nanorods also grow in the preferred orientation of [0 0 1], but do not form a network structure, probably because the high concentration of Bi makes the solution growth change from the seeded mode to self-nucleation mode [43]. As shown in Fig. 2f and i, the element distribution mapping of these two samples is characterized by energy dispersion spectrum (EDS), and the contents of chlorine element in the two precursors are 4.22 ± 0.96 at% and 3.94 ± 0.94 at%, respectively. Each element is homogeneously distributed, and there is no obvious second-phase enrichment. In addition, nitrogen adsorption and desorption experiments were carried out to analyze pore information of these as-synthesized powder (Fig. S5). The specific surface areas of HT-NN and HT-NR powder fitted by the Brunauer–Emmett–Teller (BET) equation are 16.76 m^2/g and 10.08 m^2/g respectively, indicating that the single nanorod of HT-NN is shorter and has smaller grains in the case of similar diameters. HT-NN exhibits a Barrrett–Joyner–Halenda (BJH) adsorption cumulative volume of pores of 0.056 cm^3/g, which is twice that of HT-NR (0.028 cm^3/g), suggesting that HT-NN is rich in porous structure derived from orthogonal nanorods. As a result, it is a reasonable hypothesis that some defects of HT-NN nanonetworks (such as non-flat edges) enable them to form large amounts of nanoscale voids during the stacking process, which facilitates the formation of pore structures during further sintering.

3.2. Electron microscopy analysis on SPSed monoliths

The XRD patterns of SPSed bulk specimens along different directions are shown in Fig. S1a. After the SPS process, the main diffraction peaks become narrower and sharper according to the half-height width of the strongest diffraction peak, confirming the increase of grain size. Besides, obvious difference in the intensities of the diffraction peaks between the samples perpendicular to the pressure direction and those parallel to the pressure direction indicates that the bismuth sulfide forms anisotropic ingots under pressure sintering. In the pattern of the cut plane perpendicular to the direction of pressure, the diffraction peak of the (0 0 1) crystal plane almost disappears, while the diffraction peak of the (0 0 1) plane is enhanced in surface parallel to the direction of pressure, which is estimated by Lotgering factor as following.

The Lotgering factors [44] of the bulk cleavage surfaces in different pressing directions are listed in Table 1 (the details are shown in Supplementary Note 3). The results show that both materials have strong <h k 0 > preferred orientation in the perpendicular to the pressure direction and weak < 0 0 1 > orientation in the parallel to pressure direction. It is worth noting that the Lotgering factor of HT-NN is slightly lower than that of HT-NR, which may be because HT-NN is highly nano-sized, with small and irregular grains verified by SEM images below. Clearly, extremely low thermal conductivity can be obtained in parallel directions, but the electrical properties are deteriorated by van der Waals gaps. On the contrary, the electrical conductivity is significantly improved in the vertical direction, and the thermal conductivity is higher, which is consistent with the experimental results. The XRD patterns of FL-NN and FL-NR are shown in Fig. S1b and the results are similar.

The micro and nanostructures of SPSed bulk specimens are shown in Fig. 3. Fig. 3a and b are BSE images of polished surfaces of HT-NN and HT-NR, respectively. The black spots in BSE image reflect the pore structure on the surface and deep layer (over 100 nm) of the sample, and the pore distribution between the two is in stark contrast. The pores in HT-NN are smaller and more densely distributed, while that of HT-NR are larger and sparse. Fig. 3c and d are the high-magnification SEM image of fractured surfaces of sintered monoliths perpendicular to pressure direction. The grain size of HT-NN is about 190 ± 90 nm (average density: 6.05 g/cm^3 with a standard deviation of 0.072 for over 15 samples; relative density: 89.0% ± 1%), while grain size of HT-NR is 620 ± 280 nm (average density: 6.52 g/cm^3 with a standard deviation of 0.071 for over 15 samples; relative density: 95.7% ± 1%), as shown in Fig. 3c-d insets. It can be clearly observed that the grains of HT-NN are olive-shaped, with a large grain boundary density. Meanwhile, plentiful holes can be observed in the grains of HT-NN, which is the reason for the significant decrease in its relative density. As aforementioned, the source of these holes is the void caused by the stacking of HT-NN nanonetworks. In contrast, the grains of HT-NR are mostly cuboid, whose size is much larger than that of the powder precursors, indicating that nanorods without special stacking are easy to recrystallize and form denser grains under the sintering conditions of high temperature and high pressure. In order to visually display the pore structure of HT-NN, bulk TEM samples were prepared by ion thinning technique. Fig. 3e and h are the HR-TEM images of the crystal lattice of HT-NN specimen. From Fig. 3e, the image of Bi_2S_3 crystal looking down from the *a*-axis is obtained, and the corresponding atomic arrangement information is also given in the inset. The Van der Waals gap between [BiS_3] chains can be clearly observed. To clearly display the strain field in the atomic scale, two vertical diffraction spots (0 1 0) and (0 0 1) were selected for geometric phase analysis (GPA) [45]. As shown in Fig. 3f, the distinct normal strain along strain tensors ε_{xx} indicates that [BiS_3] zigzag is distorted by Cl incorporation. Fig. 3g is the low-resolution TEM image of the HT-NN sample's thin area. The pore structure is clearly expressed by mass contrast and is very abundant, with diameters ranging from 30 nm to 100 nm. Fig. 3h shows an overview of Bi_2S_3 lattice along [0 1 0] zone axis. By taking the inverse Fourier transform of the diffraction spots on

Table 1
The Lotgering factor of (h k 0) and (0 0 1) crystal planes.

Lotgering factor	HT-NN bulk parallel	HT-NR bulk parallel	HT-NN bulk perpendicular	HT-NR bulk perpendicular
$F_{(hk0)}$	non-<h k 0 > oriented	non-<h k 0 > oriented	0.36, moderately oriented	0.62, well oriented
$F_{(001)}$	0.035, poorly oriented	0.052, poorly oriented	non-< 0 0 1 > oriented	non-< 0 0 1 > oriented

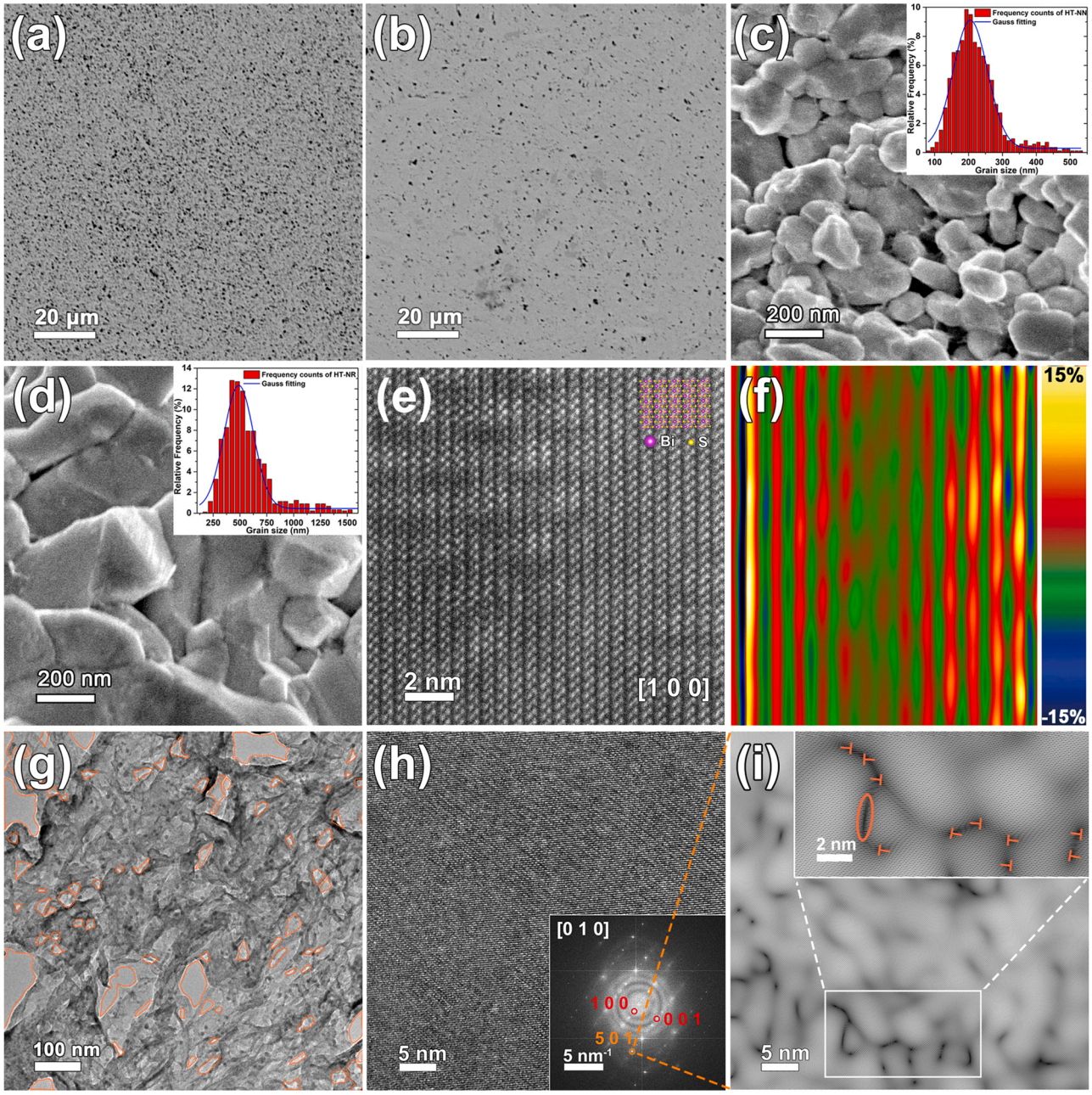

Fig. 3. Morphologies and lattice fringes of SPSed bulk samples. (a, b) Back-scattered electron (BSE) images of HT-NN and HT-NR polished surfaces, respectively; (c, d) high-magnification SEM images of fractured surfaces of HT-NN and HT-NR with related statistical chart of grain size, respectively; (e) aspherical aberration-corrected TEM (ac-TEM) image of ion-beam-thinned HT-NN specimen; (f) geometric phase analysis (GPA) of corresponding ac-TEM image (e) in the x-direction, the color scale of temperature from yellow to blue reflects a change in strain value from −15% to 15%; (g) low-resolution TEM image of a thin area in ion beam thinned specimen, and the outline of the pores are highlighted by orange dash lines; (h) HR-TEM image of HT-NN with its corresponding FFT graph; (i) inverse FFT image based on (5 0 1) diffraction spot, which shows a high density of dislocations and stacking faults.

the (5 0 1) crystal plane, it can be found that the HT-NN sample contains plenty of dislocations and stacking faults.

3.3. Synchrotron radiation SAXS study on pore structures

Although electron microscopy can visually detect the pore morphology, it lacks statistical significance. To further investigate the

statistical distribution of disconnected pores, synchrotron radiation small-angle X-ray scattering (SAXS) was used to analyze these isolated pore structures in heterogeneous electron-density systems. The optical path diagram of the SAXS experiment through synchrotron radiation X-ray is illustrated in Fig. 4a, with a two-dimensional SAXS image inserted in Fig. 4b. When a beam of X-ray irradiates a sample with uneven electron density, the scattering intensity in a small Angle range can well reflect the information of nanoscale scatterers in the material. In these porous Bi_2S_3 systems, the heterogeneous nanoscale pore structure causes the electron gas density of the system to fluctuate, which can effectively scatter X-rays. Scattering vector q is an important parameter in X-ray scattering theory, which is written as $q = 4\pi sin(\theta)/\lambda$. Fig. 4b shows the relationship between scattering intensity (I) and scattering vector (q) obtained through integrating 2-D scattering data. Clearly, HT-NN has a higher scattering intensity, which is caused by its high porosity.

Moreover, SAXS is one of the effective means to measure the fractal dimension, which can express the self-similarity and roughness of the nano-structure in samples. According to Porod formula $I(q) \propto Aq^{-\alpha}$ [46], where A is a constant and the power exponent α is the fractal dimension-related parameter. When $3 < \alpha < 4$, it indicates that the object is compact and the surface fractal exists, which can be expressed as $D_s = 6 - \alpha$ [47]. When $0 < \alpha < 3$, it suggests that the sample has a loose structure and is mass fractal, which can be depicted as $D_m = \alpha$. The α is obtained from the slope of the tangent line in log-log graphs of the

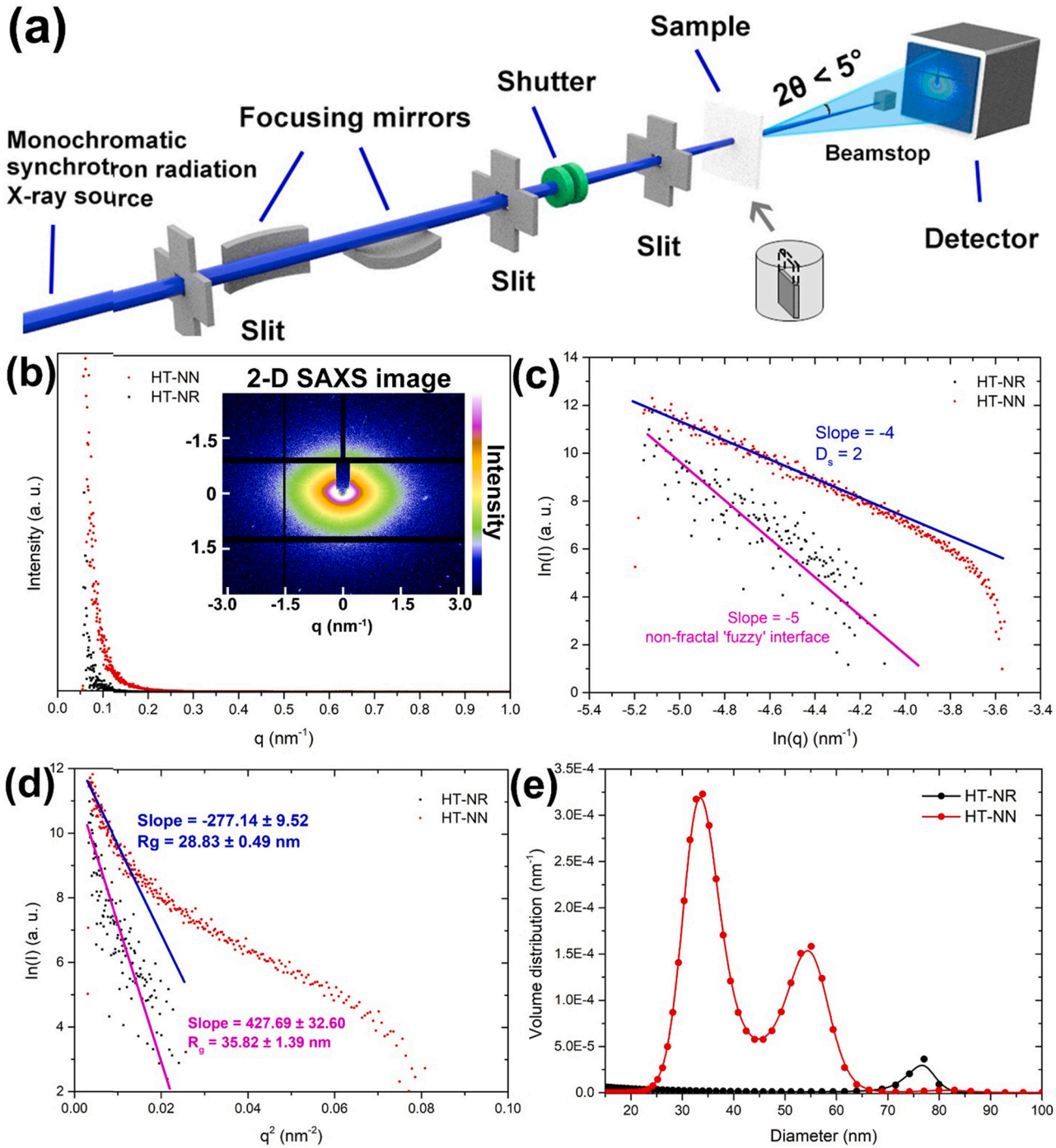

Fig. 4. (a) Schematic diagram of synchrotron radiation SAXS experiment. (b) SAXS original data (inset is a 2-D data graph of HT-NN), (c) fractal dimension curve, (d) Guinier curve, (e) pore size distribution curve of HT-NN and HT-NR.

intensity vs. scattering vector, as shown in Fig. 4c. The α of HT-NN is 4, which indicates that its D_s is 2 and the surface of the pore structure is very smooth. The slope of the characteristic straight line in HT-NR plot is − 5, which is caused by its non-fractal boundaries with gradually changed scattering length density between pores and grains [48].

Furthermore, in order to estimate the average pore size, the curve is processed by the Guinier formula [49]:

$$I(q) = I_e M n^2 e^{-\frac{q^2 R_g^2}{3}} \tag{1}$$

$$\ln I(q) = C - \frac{R_g^2}{3} q^2, \tag{2}$$

where M is the number of incoherent pores, I_e is the Thomson scattering intensity of a single electron, n is the total number of electrons in a pore, and R_g is the radius of gyration, which is an important parameter to calculate the average radius of practical pores. The radius of gyration can be obtained by fitting the slope of the Guinier plot (Fig. 4d) in the low-scattering vector region. The R_g values of HT-NN and HT-NR are 28.87 ± 0.49 nm and 35.82 ± 1.39 nm, respectively. The relation between spherical pore and R_g can be written as $R_g = \sqrt{3/5}R$. Therefore, the average pore sizes of HT-NN and HT-NR are 37.27 nm and 58.38 nm based on the spherical pore hypothesis, respectively. The Guinier curve of HT-NR has a large linear region and shows good monodispersity, while that of HT-NN indicates that the pore-size distribution is polydispersed.

The pore size distributions of two samples are calculated by the maximum entropy method [50], as shown in the following equation,

$$I(q) = \Delta\rho^2 \sum F^2(q,r) V^2(r) NP(r) dr \tag{3}$$

in which $\Delta\rho$ is the difference of scattering length density between pores and Bi_2S_3 matrix, *F(q, r)* is the form factor of the scatterer, *V(r)* is the volume of a pore with a diameter of *r*, *P(r)* is the probability size distribution of pores. The pore size distribution (PSD) curve of HT-NN and HT-NR are shown in Fig. 4e in the range of 5–90 nm. Clearly, the PSD curve of HT-NN shows a doublet peak with a pore size range from 25 nm to 65 nm, reaching the maximum volume value at 37 nm and 55 nm, respectively. That of HT-NR exhibits a unimodal distribution with a peak value of 77 nm, and its volume distribution is much smaller than HT-NN. The results of a series of SAXS analyses can confirm each other, indicating that HT-NN has smaller and more pores and a wider size distribution range, which is consistent with SEM observation results.

3.4. Thermal conductivity and Boltzmann transport equation (BTE) modeling

The nanopores and rich nanostructures characterized above have

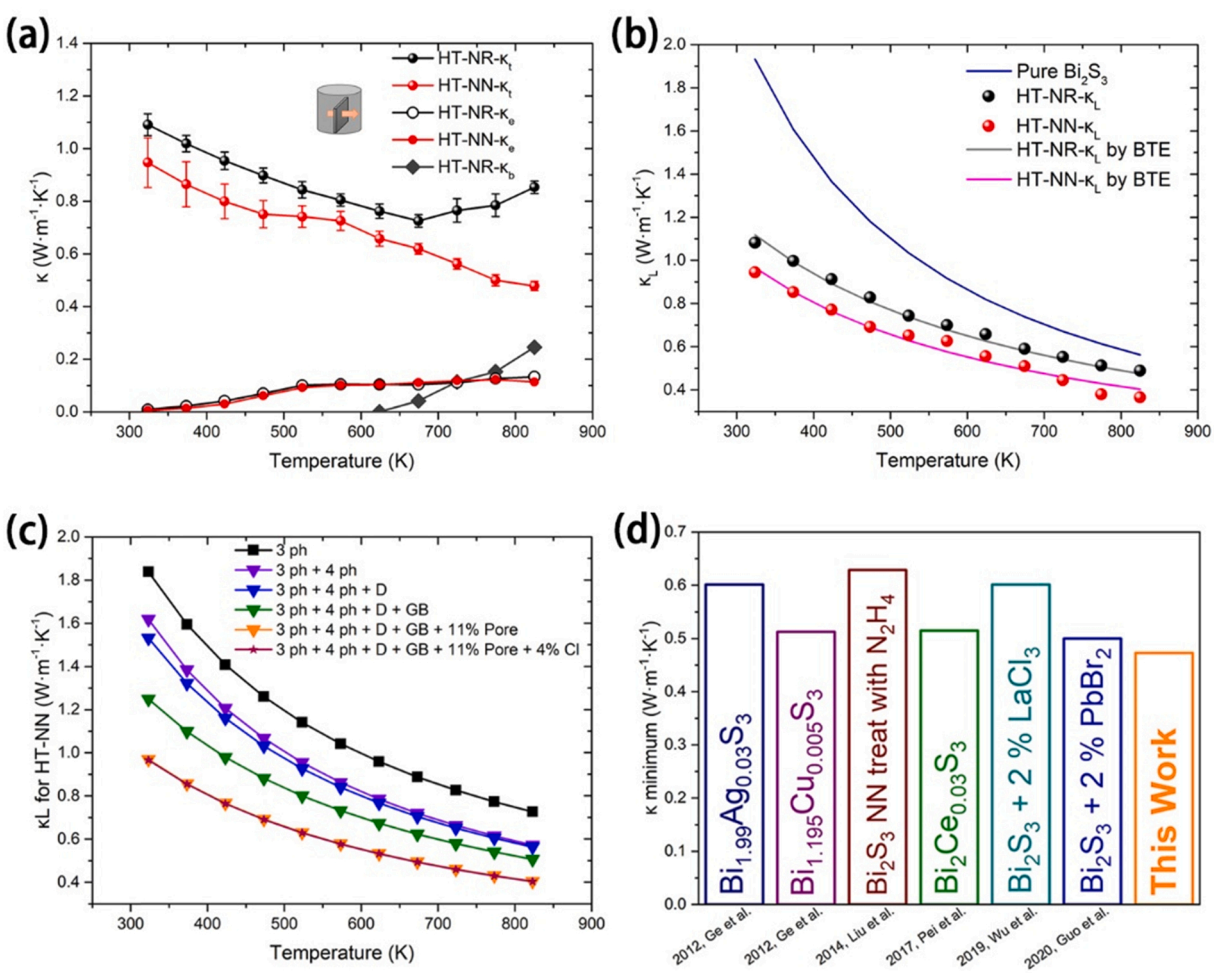

Fig. 5. Experimental and modeled thermal conductivity. (a) Total thermal conductivity (κ_t), polar-electron thermal conductivity (κ_e), and bipolar thermal conductivity (κ_b) of HT-NR; (b) experimental data (dots) of κ_L for HT-NN and HT-NR with corresponding fitted curves (solid lines) calculated via BTE model; (c) lattice thermal conductivity drop due to various phonon scattering mechanisms in HT-NN, which considered Umklapp process of three-phonon (*3-ph*) and four-phonon (*4-ph*), defects (*D*), grain boundaries (*GB*), pores in the nanoscale (*Pore*), and chlorine doping (*Cl*); (d) comparison of the lowest thermal conductivity of HT-NN with the reported values in the direction perpendicular to sinter pressure [6,8,15,37,53,54].

considerable influence on thermal conductivity. Fig. 5a shows the temperature-dependent of total thermal conductivity κ_t, which contains contributions from electrons (κ_e), bipolar electron-hole pairs (κ_b), and lattice vibrations (κ_L). It can be seen that HT-NR has clear bipolar thermal conductivity, which increases fast at high temperature, while HT-NN has almost none. Since HT-NN and HT-NR are doped to a similar extent, the changes in carrier concentration and band structure by chlorine impurities are similar. The difference in κ_b is mainly caused by the difference in the degree of scattering of minority carriers. In HT-NN samples, nanopores with tens of nanometers and highly nanosized grain boundaries and grains can scatter minor carriers more efficiently due to the wavelength of the holes is close to those nanostructures at the intrinsic region. In contrast, HT-NR is almost devoid of these nanostructures, making it weak to hole scattering and exhibiting significant bipolar thermal conductivity (the detailed discussion is included in Supplementary Note 4). According to Wiedemann-Franz law, the contribution of electrons can be expressed as $\kappa_e = L_1\sigma T$, in which L_1 is the electronic polar Lorenz number [51] calculated from the single parabolic band model (SPB, see Supplementary Note 5). The Lorenz number contributed by bipolar electron-hole pairs can be expressed as $L_2 = (\frac{k}{e})^2 \frac{b}{(b+1)^2}(\frac{E_g}{kT} + 4)^2$ [52]. We fit κ_b from this equation such that $\kappa_t = \kappa_e + \kappa_b + \kappa_L$ is satisfied (the details are depicted in Supplementary Note 6).

To gain insight into the lattice thermal conductivity and understand the relative importance of various thermal resistance mechanisms, we fit the experimental data based on the BTE model with the full phonon dispersion relation obtained by density functional theory (DFT) calculations (see Supplementary Note 7 and 8 for details). In the fitting process, we have considered the intrinsic phonon-phonon anharmonic scattering and extrinsic phonon-grain boundary scattering, phonon-chlorine impurity scattering, phonon-nanopore scattering, and phonon-other defect scattering. Since all the phonon-extrinsic scattering mechanisms do not present strong temperature dependence [30,55,56], the faster-than-T^{-1} decreasing trend of κ_L with temperature is plausibly due to four-phonon scattering [57–59]. Since 2016, four-phonon has been proven to be critical in many simple crystals [33,57–68]. Four-phonon scattering, as a high-order phonon anharmonic scattering is usually important for low-thermal conductivity materials, which is exactly the case of thermoelectric materials. Therefore, in very recent years, many thermoelectric materials have been found to have critical four-phonon scattering [32–35]. More importantly, four-phonon scattering becomes even more important as temperature increases. As a result, four-phonon scattering plays a significant role in thermoelectrics [60]. To support our hypothesis, we have calculated the three-phonon and four-phonon scattering phase spaces based on the phonon dispersion relation by DFT (Fig. S7). The four-phonon scattering phase space is not small compared to the three-phonon scattering. The weighted four-phonon scattering phase space is even larger. Although the scattering phase space is still not the same as scattering rates, they are indirect evidence for strong four-phonon scattering. Note that the modeling is based on relaxation time approximation and is not able to include the phonon boundary transmission phenomenon that is captured in Monte Carlo simulations [69]. Regarding the impact of nanopores, we not only consider their scattering with phonons but also include their reduction to heat capacity (by effective medium approximation). The grain boundary, nanopore, and chlorine impurity scatterings are calculated by using the experimentally characterized grain sizes, porosity, pore sizes, and impurity densities, respectively. The phonon-other defect scattering is a fitting parameter that implicitly includes all other defects such as lattice distortions and dislocations whose densities are difficult to count. The fitted results are shown in Fig. 5b, which agree well with experimental data when bipolar thermal conductivity is negligible. The lattice thermal conductivity reductions by various scattering mechanisms in HT-NN are shown in Fig. 5c. The HT-NN sample experiences a larger impact by nanopores than that in the HT-NR sample (Fig. S8). In addition, we have compared the minimum total thermal conductivity of our HT-NN sample with the reported values prepared by a variety of methods in the Bi_2S_3 system, indicating that the κ_{min} of our porous Bi_2S_3 is lower than that of most materials in the same direction (Fig. 5d).

3.5. Electrical transport properties

The temperature-dependent electrical performances of two bulk specimens (nanonetwork and randomly oriented nanorod) in the direction perpendicular to the sintering pressure are shown in Fig. 6. Undoped Bi_2S_3 usually has a low intrinsic carrier concentration but high mobility of over 10 $cm^2V^{-1}s^{-1}$ [7,36]. Compared with other pristine Bi_2S_3 samples, the room temperature carrier concentration of our HT-NN and HT-NR increased significantly by two orders of magnitude, reaching 10^{19}-10^{20} cm^{-3} (the related parameters are shown in Table 2), which is attributed to the heavy doping of chlorine. Both XPS and EPMA spectra proved the existence of Cl^-, the details will be discussed in the next section. The mobilities of the two samples are lower than that of Bi_2S_3 doped by other methods, which may be due to the strong scattering of carrier transport by abundant pores and grain boundaries.

The Seebeck coefficient with error bar is displayed as Fig. 6a. Negative Seebeck coefficients indicate that electrons are the majority carriers in Bi_2S_3 system. The absolute Seebeck coefficient increases linearly with rising temperature from 323 K to 673 K, then plateaus to about 230 μV/K. According to $= \gamma - \ln n$, where γ is the scattering factor and n is the carrier concentration. Since n is on the order of 10^{20} cm^{-3} in the high-temperature region, the absolute values of Seebeck coefficients of both two specimens are much lower than the none-doped Bi_2S_3 reported in some other literature [6,8,14]. Based on Mott expression, the Seebeck coefficient is depicted as $S = (\pi^2 k_B^2 T/3e)(dn(E)/nd(E)+d\mu(E)/\mu d(E))_{E=Ef}$, also indicating that the reduction of S attributes to the huge increase of carrier concentration. The variation trend of Seebeck coefficients and carrier concentrations of the two samples are the same and very close (Fig. 6c), indicating that the scattering factors of the two samples are roughly the same. The Seebeck coefficient of HT-NR decreases gently after 723 K, which agrees with the change of its thermal conductivity at > 723 K and is caused by the bipolar diffusion effect.

The electrical conductivity as a function of temperature is shown in Fig. 6b, which can be expressed as $\sigma = ne\mu$, where n is carrier concentration, e is the elementary charge, and μ is carrier mobility. In general, the electrical conductivity of HT-NR is slightly higher than that of HT-NN and the main trend of conductivity is to increase first and then decrease, which is attributed to the multiple scattering mechanisms of charge carriers. In low-temperature region (323–523 K), the conductivity of both increases exponentially with temperature, and grain boundary scattering ($\mu \propto T^{1.9}$) is the dominant mechanism [9,36]. By calculating a dimensionless determinant α_{BD} [71], the possibility of scattering from ionized impurities is ruled out (the details are expressed in Supplementary note 9). The rapid increase of conductivity before 423 K is attributed to the rapid increase of mobility, which indicates that there is a large potential barrier (E_b) at the grain boundary to inhibit carrier transport. According to the formula of σ dominated by grain boundary scattering proposed by Seto [72], we fit the E_b of the two samples, which are both high values of 170 meV (Fig. S9). As the temperature rises from room temperature to 523 K, more and more high-energy carriers are excited and break through that interfacial barrier, making the conductivity increase rapidly. Due to the high density of HT-NN grain boundary, the grain-boundary scattering of the carrier is stronger, and the mobility is lower (Fig. 6c inset), resulting in the conductivity of HT-NN being slightly lower than that of HT-NR with less grain boundary. When the temperature reaches 523 K, an inflection point appears in the conductivity curve, where the grain boundary scattering and acoustic phonon scattering reach equilibrium. Although the carrier concentration still rises slowly, phonon scattering ($\mu \propto T^{-1.8}$ with an exponent close to −1.5) becomes the dominant factor [9,73], leading to the decrease of mobility and finally the decrease of

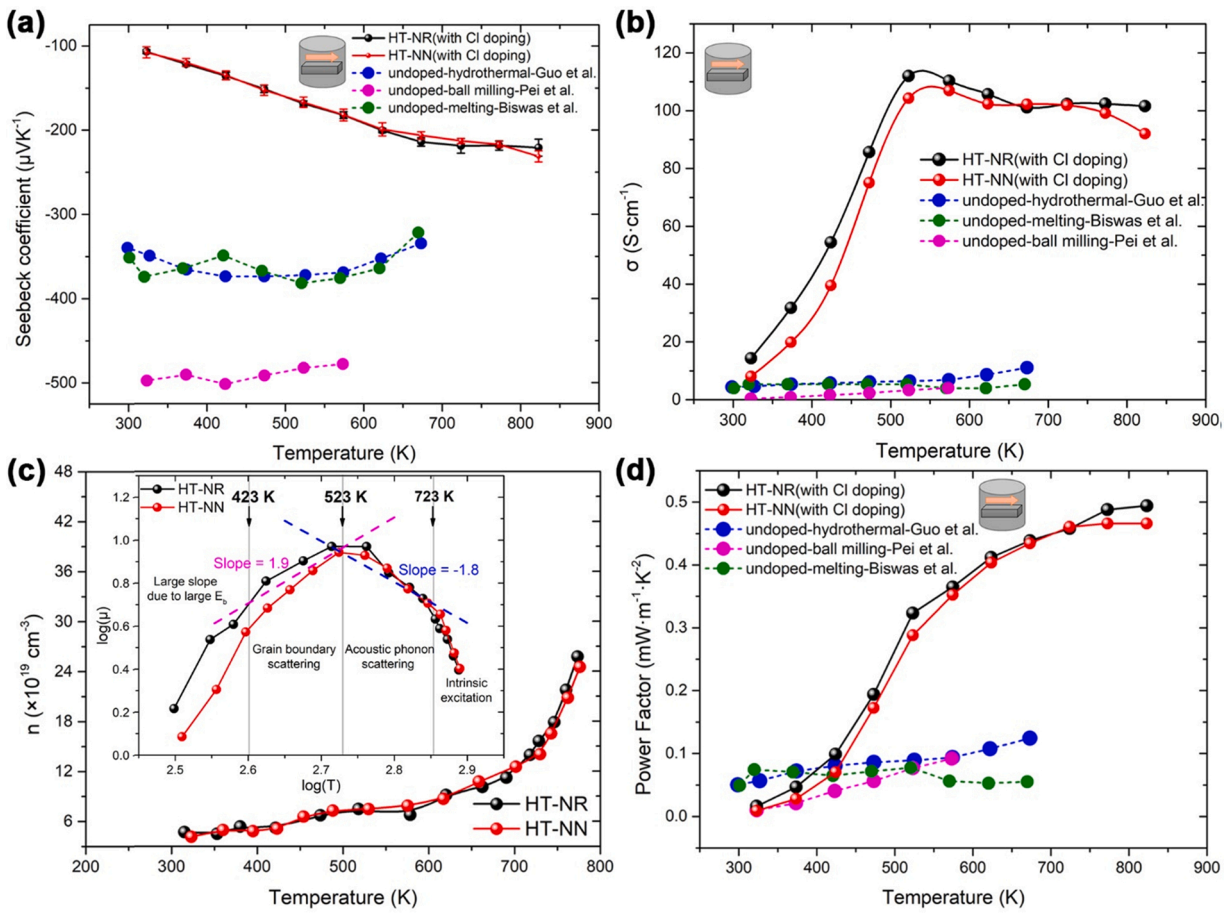

Fig. 6. Temperature-dependent electrical properties of HT-NN and HT-NR: (a) Seebeck coefficient, (b) electrical conductivity, (c) carrier concentration (n) plot with an inset of log(μ) vs. log(T) curve, and (d) power factor with the performance curves of undoped Bi_2S_3 prepared through three different methods (hydrothermal, melting, and ball milling methods) in the perpendicular direction of sintering pressure [6,7,36].

Table 2
The room-temperature physical properties of HT-NN and HT-NR. The density (ρ_0) of single-crystal Bi_2S_3 is 6.78 g·cm^{-3} [70]. The hall data of pristine Bi_2S_3 is based on undoped samples from the literature.

Abbreviation	Cl content (atomic %)	n_e (*10^{19} cm^{-3})	μ (cm^2 V^{-1} s^{-1})	m^*_{DOS} (m_e)	ρ (g cm^{-3})	ρ/ρ0
Bi_2S_3 [36]	0.00%	0.045	38	0.27	–	–
HT-NN	3.47%	4.06	2.01	0.62	6.056 ± 0.072	89.0% ± 1.1%
HT-NR	3.67%	4.71	2.98	0.68	6.514 ± 0.071	95.7% ± 1.0%

conductivity with respect to T after 523 K. Finally, the conductivity of HT-NR recovered mildly in the high-temperature region (723–823 K), which is attributed to the intrinsic excitation of the material.

The power factors ($S^2\sigma$) of the two samples gradually rise with the increase of temperature, as shown in Fig. 6d. As HT-NR has a larger grain size, smaller grain boundary density, and fewer pores, its carrier mobility is slightly better than that of HT-NN, resulting in a higher power factor in the high-temperature region, which reaches 0.50 mWm^{-1}K^{-2} at 823 K. While HT-NN also has a high value of about 0.47 mWm^{-1}K^{-2} at 823 K.

3.6. Cl doping and band structures calculations

EPMA is applied to determine the composition of each element in these Cl-doped Bi_2S_3 systems. The results of EPMA elemental mapping and the element content in ten different regions are shown in Fig. S10. The mapping shows that Bi, S, and Cl are evenly distributed, and no obvious second phase exists. After averaging and normalization, the compositions of HT-NN and HT-NR are expressed as $Bi_2S_3Cl_{0.18}$ and $Bi_2S_{2.98}Cl_{0.19}$, respectively. The surface element environmental of the fractured bulk surface was studied by XPS, as shown in Fig. 7a-b. It can be observed that the peaks in the spectra belong to bismuth, sulfur, chlorine, carbon, and oxygen, and the absence of photoelectron peaks of other elements in the survey spectra (Fig. S11) indicates that the sample is of pure phase.

Fig. 7a shows the high-resolution XPS spectra of Bi 4 f peak, which is the photoelectron peak of Bi 4 $f_{5/2}$ and Bi 4 $f_{7/2}$ at 163.85 eV and 158.55 eV, respectively. Through careful comparison, the peak positions of the two samples are almost the same. It is worth mentioning that the Bi 4 f splitting peaks of both samples had shoulder peaks, which are located at 164.45 eV and 159.25 eV, respectively. The shift of Bi 4 f is due to the doping of more electronegative chlorine, which makes Bi more electrically positive and improves its binding energy [74]. While the doublet with lower binding energy is Bi-S bond in Bi_2S_3 system [75]. Peaks at 162.45 eV and 161.30 eV correspond to the S 2p band, which are located between the splitting peaks of Bi 4 f. From Fig. 7b, the binding energies at 198 eV and 199.8 eV are assigned to Cl $2p_{3/2}$ and Cl $2p_{1/2}$, respectively. The binding energy of less than 200 eV indicates the existence of Cl in the form of Bi-Cl metal-chlorine bond [74]. According to the research results of EPMA and XPS, no matter for the distribution of elements in the deep layer of the block or the chemical environment information on the grain surface, Cl was successfully doped into the

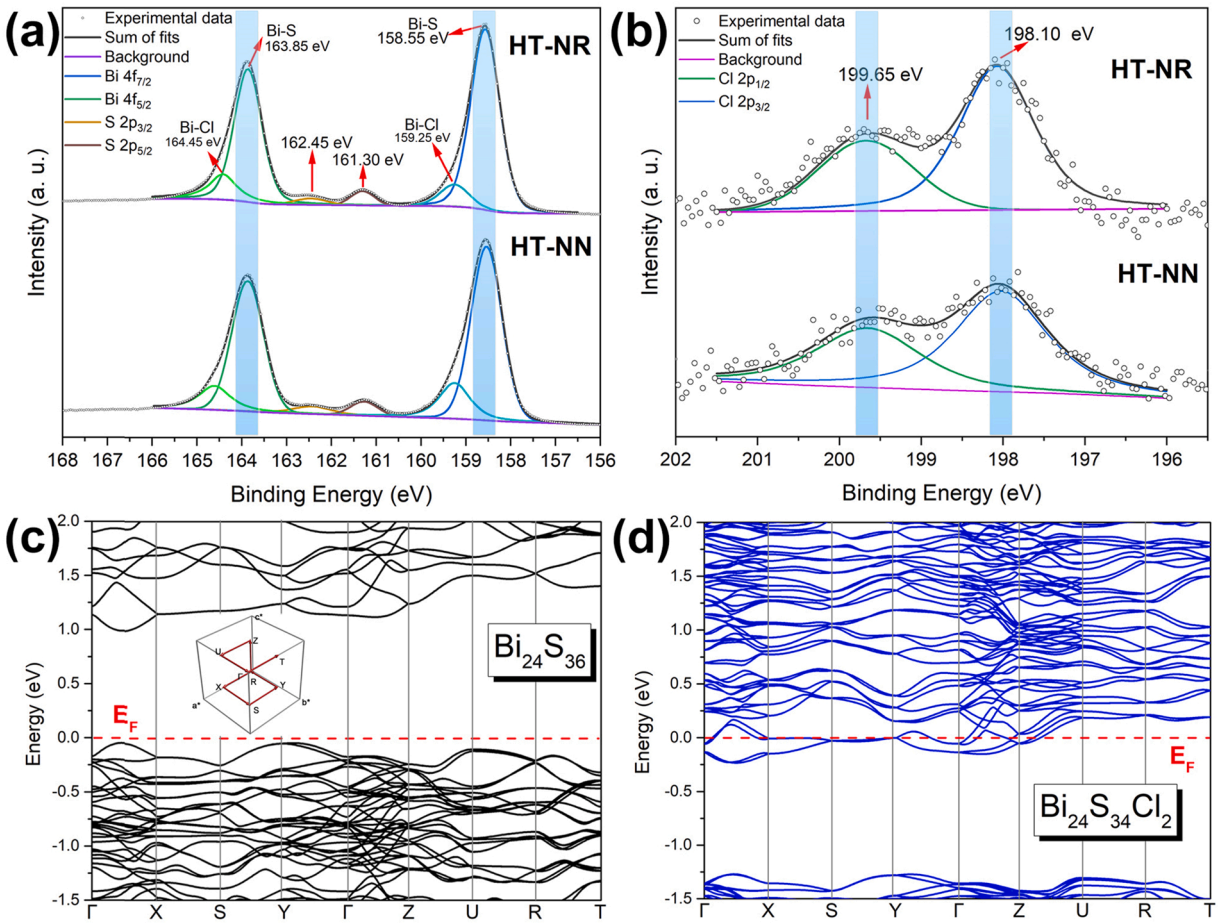

Fig. 7. XPS spectra of HT-NN and HT-NR bulk sample: (a) Bi 4 f and S2p; (b) Cl 2p; (c) calculated band structure of pristine Bi_2S_3 supercell ($Bi_{24}S_{36}$) with the inset illustrating its 1st Brillion zone; (d) band structure of 3% Cl-doped Bi_2S_3 ($Bi_{24}S_{34}Cl_2$).

Bi_2S_3 lattice with uniform distribution.

Considering the wide bandgap and low carrier concentration of pristine Bi_2S_3, strong n-type dopants are often used for doping, especially in the form of heavy metal halides. Since chloride ion is not easy to have a side reaction with the reactants, and the ion radius is close to that of sulfur, it is selected in this work to replace S and supply electron. To gain insight into the electronic structure of Bi_2S_3 doped with Cl, we conducted first-principles density functional theory (DFT) calculations. We take into consideration the spin-orbit coupling (SOC) since the previous first-principles studies have demonstrated the importance of SOC in determining the band structure of bismuth-based compounds [76,77]. The band structure of pristine Bi_2S_3 $1 \times 1 \times 3$ supercell is calculated as shown in Fig. 7a with a bandgap of 1.03 eV, which indicates a general underestimation of the bandgap by PBE exchange-correlation functional [78,79]. Both the valence band maxima (VBM) and conduction band minima (CBM) are close to the Γ point, where the CBM is located between Γ and X point, and the VBM is situated between Γ and Y point, indicating that Bi_2S_3 is a typical indirect bandgap semiconductor. Besides, it can also be observed that multiple bands with their energy levels very close to VBM and CBM exist on Γ-X path and Γ-Z path, respectively. Such a multi-minima band structure may promote electron transport. However, due to the large bandgap, Bi_2S_3's intrinsic carrier concentration is very low, which leads to its poor conductivity. We calculated a series of formation energies of Cl-substitution doped configurations. The results showed that the substitution of S_2 site required the lowest energy (Fig. S13 and Table S2). Then, we simulated the influence of increasing Cl doping concentration on the band structure as shown in Figs. 7d and S12, and the Cl doping concentrations are 1.7 at% and 3.3 at%, respectively. The incorporation of Cl pushes the Fermi level into the conduction band and the material becomes a degenerate semiconductor, which greatly increases the carrier concentration of the system. Compared with the band structure of pure Bi_2S_3, that of Cl doped one is largely unchanged, and the main difference is the band splitting at VBM and CBM, which is attributed to the doping of Cl breaking the lattice symmetry of the pure phase.

Based on the aforementioned data, the calculated *ZT* is shown in Fig. 8a. Due to the chlorine doping, the carrier concentrations of the two samples are greatly increased, which compensates for the deterioration of carrier mobility by pore structure and grain boundary and both samples reach high *ZT* values. Noticeably, the *ZT* of the sample with more pores reaches 0.81 at 823 K, which is 60% higher than that of the sample with lower porosity, indicating that the porous structure can efficiently improve *ZT* in Bi_2S_3 system. In addition, this is the first time that Bi_2S_3-based TE material has achieved a state-of-the-art *ZT* in the high-temperature region (773–823 K, Fig. 1d), extending its application temperature range as n-type TE material. The related thermogravimetric test and thermoelectric performance cycle test are shown in Fig. S15, further confirming the thermal stability of our materials.

We have also calculated a theoretical thermo-to-electric conversion efficiency based on

$$\eta = \frac{T_h - T_c}{T_h}\left[\frac{\sqrt{1+ZT_{avg}}-1}{\sqrt{1+ZT_{avg}}+\frac{T_c}{T_h}}\right], \quad (4)$$

where T_h is the temperature of the hot end, T_c is the temperature of the cold end, and ZT_{avg} is the average value of *ZT*, which can be depicted in the following equation,

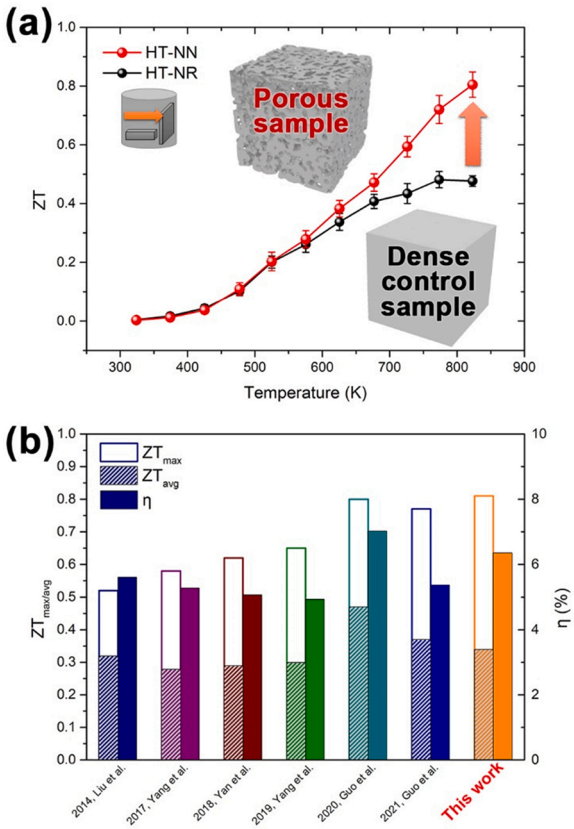

Fig. 8. (a) Temperature-dependent *ZT* value of HT-NN and HT-NR; (b) comparison of maximum *ZT* (ZT_{max}), average *ZT* (ZT_{avg}), and theoretical thermoelectric conversion efficiency (η) of Bi_2S_3 systems with excellent performance in recent years [6,10,12,36,37,80].

$$ZT_{avg} = \frac{1}{T_h - T_c}\int_{T_c}^{T_h} ZT \quad dT. \tag{5}$$

According to Eqs. (4) and (5), the ZT_{avg} and T_h-T_c are critical to conversion efficiency. Although ZT_{avg} of the sample is not the highest, the large temperature difference that samples can withstand increases the η. The theoretical conversion efficiency of our HT-NN reaches 6.3%, which is the highest value of Bi_2S_3 prepared by solution methods and is also good in high-performance Bi_2S_3 materials in recent years.

4. Conclusion

In summary, we have prepared high-performance Bi_2S_3-based thermoelectric material from the solution-synthesized porous precursor, which has the advantages of simple manipulation, short time, and low energy consumption. Two kinds of powder samples with different morphologies, namely the networked and randomly oriented nanorod, were synthesized by hydrothermal method with the same reactants. Network nanodiscs (HT-NN) have a finer grain size and more nanopores after the SPS process, resulting in reduced lattice thermal conductivity and lower density of the material. The lower relative density makes it more portable and promising for special applications, such as radioisotope thermoelectric generators (RTG). Its maximum *ZT* value is 0.81 at 823 K, which is 60% higher than the dense control sample (HT-NR) and is among the highest *ZT* values reported in Bi_2S_3 materials. Compared with previously reported Bi_2S_3-based TE materials, this work also broadens the application temperature range of the Bi_2S_3 system, providing a new strategy for the preparation of high-performance, eco-friendly and portable thermoelectric devices.

CRediT authorship contribution statement

Kangpeng Jin: Conceptualization, Investigation, Methodology, Data curation, Formal analysis, Visualization, Software, Validation, Writing – original draft. **Janak Tiwari:** Formal analysis, Software, Writing – original draft. **Tianli Feng:** Conceptualization, Software, Resources, Writing – review & editing, Supervision. **Yue Lou:** Resources, Writing – review & editing, Supervision. **Biao Xu:** Conceptualization, Resources, Writing – review & editing, Supervision, Project administration, Funding acquisition.

Declaration of Competing Interest

The authors declare that they have no known competing financial interests or personal relationships that could have appeared to influence the work reported in this paper.

Acknowledgments

B.X. thanks financial supports from the Jiangsu Specially Appointed Professorship and Innovation and Entrepreneurship Talents in Jiangsu Province (China). Y.L. thanks financial supports from the Doctor of Entrepreneurship and Innovation in Jiangsu Province of China (JSSCBS20210215). J.T. and T.F. acknowledge the support from the University of Utah (USA). K.J. acknowledges the great help from Mengting Xu and Prof. Liangwei Fu.

Appendix A. Supplementary material

Supplementary data associated with this article can be found in the online version at doi:10.1016/j.nanoen.2022.107478.

References

[1] G. Tan, L.D. Zhao, M.G. Kanatzidis, Rationally designing high-performance bulk thermoelectric materials, Chem. Rev. 116 (2016) 12123–12149.
[2] J. He, T.M. Tritt, Advances in thermoelectric materials research: Looking back and moving forward, Science 357 (2017) eaak9997.
[3] P. Larson, V.A. Greanya, W.C. Tonjes, R. Liu, S.D. Mahanti, C.G. Olson, Electronic structure of Bi_2X_3 (X—S,Se,T) compounds: Comparison of theoretical calculations with photoemission studies, Phys. Rev. B 65 (2002), 085108.
[4] J. Ni, Y. Zhao, T. Liu, H. Zheng, L. Gao, C. Yan, L. Li, Strongly coupled Bi_2S_3@CNT hybrids for robust lithium storage, Adv. Energy Mater. 4 (2014) 1400798.
[5] M. Bernechea, Y. Cao, G. Konstantatos, Size and bandgap tunability in Bi_2S_3 colloidal nanocrystals and its effect in solution processed solar cells, J. Mater. Chem. A 3 (2015) 20642–20648.
[6] J. Guo, Y.X. Zhang, Z.Y. Wang, F. Zheng, Z.-H. Ge, J. Fu, J. Feng, High thermoelectric properties realized in earth-abundant Bi_2S_3 bulk via carrier modulation and multi-nano-precipitates synergy, Nano Energy 78 (2020), 105227.
[7] K. Biswas, L.-D. Zhao, M.G. Kanatzidis, Tellurium-free thermoelectric: the anisotropic n-type semiconductor Bi_2S_3, Adv. Energy Mater. 2 (2012) 634–638.
[8] J. Pei, L.J. Zhang, B.P. Zhang, P.P. Shang, Y.-C. Liu, Enhancing the thermoelectric performance of $Ce_xBi_2S_3$ by optimizing the carrier concentration combined with band engineering, J. Mater. Chem. C 5 (2017) 12492–12499.
[9] W.T. Ji, X.L. Shi, W.D. Liu, H.L. Yuan, K. Zheng, B.A. Wan, W.X. Shen, Z.F. Zhang, C. Fang, Q.Q. Wang, L.C. Chen, Y.W. Zhang, X.P. Jia, Z.G. Chen, Boosting the thermoelectric performance of n-type Bi_2S_3 by hierarchical structure manipulation and carrier density optimization, Nano Energy 87 (2021), 106171.
[10] J. Yang, G. Liu, J. Yan, X. Zhang, Z. Shi, G. Qiao, Enhanced the thermoelectric properties of n-type Bi_2S_3 polycrystalline by iodine doping, J. Alloy. Compd. 728 (2017) 351–356.
[11] Y.-X. Zhang, Z.-H. Ge, J. Feng, Enhanced thermoelectric properties of Cu1.8S via introducing Bi2S3 and Bi2S3@Bi core-shell nanorods, J. Alloy. Compd. 727 (2017) 1076–1082.
[12] J. Yang, J. Yan, G. Liu, Z. Shi, G. Qiao, Improved thermoelectric properties of n-type Bi_2S_3 via grain boundaries and in-situ nanoprecipitates, J. Eur. Ceram. Soc. 39 (2019) 1214–1221.
[13] X. Du, R. Shi, Y. Guo, Y. Wang, Y. Ma, Z. Yuan, Enhanced thermoelectric properties of $Pb_{1-x}Bi_xS$ prepared with hydrothermal synthesis and microwave sintering, Dalton Trans. 46 (2017) 2129–2136.
[14] J. Guo, Q. Lou, Y. Qiu, Z.Y. Wang, Z.H. Ge, J. Feng, J. He, Remarkably enhanced thermoelectric properties of Bi_2S_3 nanocomposites via modulation doping and grain boundary engineering, Appl. Surf. Sci. 520 (2020), 146341.
[15] Y. Wu, Q. Lou, Y. Qiu, J. Guo, Z.Y. Mei, X. Xu, J. Feng, J. He, Z.H. Ge, Highly enhanced thermoelectric properties of nanostructured Bi_2S_3 bulk materials via

carrier modification and multi-scale phonon scattering, Inorg. Chem. Front. 6 (2019) 1374–1381.
[16] Y. Chang, Q.L. Yang, J. Guo, J. Feng, Z.H. Ge, Enhanced thermoelectric properties of Bi_2S_3 polycrystals through an electroless nickel plating process, RSC Adv. 9 (2019) 23029–23035.
[17] Y. Wu, J. Pei, R. Zhang, Z.-C. Huang, Z. Zhao, B.P. Zhang, Temperature gradient cooling technique: boosting high power factor of Bi_2S_{3+x} thermoelectric material, J. Alloy. Compd. 830 (2020), 154451.
[18] M.-H. Sun, S.-Z. Huang, L.-H. Chen, Y. Li, X.-Y. Yang, Z.-Y. Yuan, B.L. Su, Applications of hierarchically structured porous materials from energy storage and conversion, catalysis, photocatalysis, adsorption, separation, and sensing to biomedicine, Chem. Soc. Rev. 45 (2016) 3479–3563.
[19] M. Dusselier, M.E. Davis, Small-pore zeolites: synthesis and catalysis, Chem. Rev. 118 (2018) 5265–5329.
[20] G. Singh, J. Lee, A. Karakoti, R. Bahadur, J. Yi, D. Zhao, K. AlBahily, A. Vinu, Emerging trends in porous materials for CO_2 capture and conversion, Chem. Soc. Rev. 49 (2020) 4360–4404.
[21] G. Cai, P. Yan, L. Zhang, H.C. Zhou, H.L. Jiang, Metal–organic framework-based hierarchically porous materials: synthesis and applications, Chem. Rev. 121 (2021) 12278–12326.
[22] M. Osiak, H. Geaney, E. Armstrong, C. O'Dwyer, Structuring materials for lithium-ion batteries: advancements in nanomaterial structure, composition, and defined assembly on cell performance, J. Mater. Chem. A 2 (2014) 9433–9460.
[23] E. Armstrong, C. O'Dwyer, Artificial opal photonic crystals and inverse opal structures – fundamentals and applications from optics to energy storage, J. Mater. Chem. C 3 (2015) 6109–6143.
[24] W. Lu, Z. Yuan, Y. Zhao, H. Zhang, H. Zhang, X. Li, Porous membranes in secondary battery technologies, Chem. Soc. Rev. 46 (2017) 2199–2236.
[25] T. Wagner, S. Haffer, C. Weinberger, D. Klaus, M. Tiemann, Mesoporous materials as gas sensors, Chem. Soc. Rev. 42 (2013) 4036–4053.
[26] C. Zhu, D. Du, A. Eychmüller, Y. Lin, Engineering ordered and nonordered porous noble metal nanostructures: synthesis, assembly, and their applications in electrochemistry, Chem. Rev. 115 (2015) 8896–8943.
[27] T.G. Novak, K. Kim, S. Jeon, 2D and 3D nanostructuring strategies for thermoelectric materials, Nanoscale 11 (2019) 19684–19699.
[28] O. Delaire, A.F. May, M.A. McGuire, W.D. Porter, M.S. Lucas, M.B. Stone, D. L. Abernathy, V.A. Ravi, S.A. Firdosy, G.J. Snyder, Phonon density of states and heat capacity of $La_{3-x}Te_4$, Phys. Rev. B 80 (2009), 184302.
[29] K. Zhao, H. Duan, N. Raghavendra, P. Qiu, Y. Zeng, W. Zhang, J. Yang, X. Shi, L. Chen, Solid-state explosive reaction for nanoporous bulk thermoelectric materials, Adv. Mater. 29 (2017) 1701148.
[30] B. Xu, T. Feng, Z. Li, S.T. Pantelides, Y. Wu, Constructing highly porous thermoelectric monoliths with high-performance and improved portability from solution-synthesized shape-controlled nanocrystals, Nano Lett. 18 (2018) 4034–4039.
[31] M. Hong, Y. Wang, S. Xu, X. Shi, L. Chen, J. Zou, Z.-G. Chen, Nanoscale pores plus precipitates rendering high-performance thermoelectric $SnTe_{1-x}Se_x$ with refined band structures, Nano Energy 60 (2019) 1–7.
[32] F. Liu, P. Parajuli, R. Rao, P.C. Wei, A. Karunarathne, S. Bhattacharya, R. Podila, J. He, B. Maruyama, G. Priyadarshan, J.R. Gladden, Y.Y. Chen, A.M. Rao, Phonon anharmonicity in single-crystalline SnSe, Phys. Rev. B 98 (2018), 224309.
[33] Y. Xia, Revisiting lattice thermal transport in PbTe: the crucial role of quartic anharmonicity, Appl. Phys. Lett. 113 (2018), 073901.
[34] J. Sun, C. Zhang, Z. Yang, Y. Shen, M. Hu, Q. Wang, Four-phonon scattering effect and two-channel thermal transport in two-dimensional paraelectric SnSe, ACS Appl. Mater. Interfaces 14 (2022) 11493–11499.
[35] L. Xie, J.H. Feng, R. Li, J.Q. He, First-principles study of anharmonic lattice dynamics in low thermal conductivity $AgCrSe_2$: evidence for a large resonant four-phonon scattering, Phys. Rev. Lett. 125 (2020), 245901.
[36] J. Guo, J. Yang, Z.H. Ge, B. Jiang, Y. Qiu, Y.K. Zhu, X. Wang, J. Rong, X. Yu, J. Feng, J. He, Realizing high thermoelectric performance in earth-abundant Bi_2S_3 bulk materials via halogen acid modulation, Adv. Funct. Mater. 31 (2021) 2102838.
[37] W. Liu, C.F. Guo, M. Yao, Y. Lan, H. Zhang, Q. Zhang, S. Chen, C.P. Opeil, Z. Ren, Bi_2S_3 nanonetwork as precursor for improved thermoelectric performance, Nano Energy 4 (2014) 113–122.
[38] Z. Liu, Y. Pei, H. Geng, J. Zhou, X. Meng, W. Cai, W. Liu, J. Sui, Enhanced thermoelectric performance of Bi_2S_3 by synergistical action of bromine substitution and copper nanoparticles, Nano Energy 13 (2015) 554–562.
[39] H. Chen, T. Huang, S. Zheng, T. Fang, L. Wang, Enhancing thermoelectric performance through one-pot solution phase synthesis of Bi_2S_3 nanobundles, Mater. Lett. 185 (2016) 67–71.
[40] D.P. Wong, W.L. Chien, C.Y. Huang, C.E. Chang, A. Ganguly, L.M. Lyu, J.S. Hwang, L.C. Chen, K.H. Chen, Enhanced thermoelectric performance in a percolated bismuth sulfide composite, RSC Adv. 6 (2016) 98952–98955.
[41] Z.H. Ge, P. Qin, D. He, X. Chong, D. Feng, Y.H. Ji, J. Feng, J. He, Highly enhanced thermoelectric properties of Bi/Bi_2S_3 nanocomposites, ACS Appl. Mater. Interfaces 9 (2017) 4828–4834.
[42] L. Li, N. Sun, Y. Huang, Y. Qin, N. Zhao, J. Gao, M. Li, H. Zhou, L. Qi, Topotactic transformation of single-crystalline precursor discs into disc-like Bi_2S_3 nanorod networks, Adv. Funct. Mater. 18 (2008) 1194–1201.
[43] F. Meng, S.A. Morin, A. Forticaux, S. Jin, Screw dislocation driven growth of nanomaterials, Acc. Chem. Res. 46 (2013) 1616–1626.
[44] F.K. Lotgering, Topotactical reactions with ferrimagnetic oxides having hexagonal crystal structures—I, J. Inorg. Nucl. Chem. 9 (1959) 113–123.
[45] M.J. Hÿtch, E. Snoeck, R. Kilaas, Quantitative measurement of displacement and strain fields from HREM micrographs, Ultramicroscopy 74 (1998) 131–146.
[46] G. Porod, Die Röntgenkleinwinkelstreuung von dichtgepackten kolloiden Systemen, Kolloid-Z. 124 (1951) 83–114.
[47] F. Xia, J. Zhao, B.E. Etschmann, J. Brugger, C.J. Garvey, C. Rehm, H. Lemmel, J. Ilavsky, Y.S. Han, A. Pring, Characterization of porosity in sulfide ore minerals: a USANS/SANS study, Am. Mineral. 99 (2014) 2398–2404.
[48] L.M. Anovitz, D.R. Cole, Analysis of the pore structures of shale using neutron and X-ray small angle scattering, Geol. Carbon Storage (2018) 71–118.
[49] C.E. Williams, R.P. May, A. Guinier, Small-angle scattering of X-rays and neutrons, in: Eric Lifshin (Ed.), X-ray Characterization of Materials, WILEY-VCH Verlag GmbH, 1999, pp. 211–254. ⟨https://doi.org/10.1002/9783527613748.ch4⟩.
[50] J. Potton, G. Daniell, B. Rainford, A new method for the determination of particle size distributions from small-angle neutron scattering measurements, J. Appl. Crystallogr. 21 (1988) 891–897.
[51] C.J. Glassbrenner, G.A. Slack, Thermal conductivity of silicon and germanium from 3°K to the melting point, Phys. Rev. 134 (1964) A1058–A1069.
[52] J.R. Drabble, H.J. Goldsmid. Thermal Conduction in Semiconductors, Pergamon Press, Oxford, 1961, https://doi.org/10.1002/bbpc.19620660617.
[53] Z.H. Ge, B.-P. Zhang, Y.Q. Yu, P.-P. Shang, Fabrication and properties of $Bi_{2-x}Ag_{3x}S_3$ thermoelectric polycrystals, J. Alloy. Compd. 514 (2012) 205–209.
[54] Z.H. Ge, B.P. Zhang, Y. Liu, J.F. Li, Nanostructured $Bi_{2-x}Cu_xS_3$ bulk materials with enhanced thermoelectric performance, Phys. Chem. Chem. Phys. 14 (2012) 4475–4481.
[55] B. Xu, T. Feng, Z. Li, L. Zhou, S.T. Pantelides, Y. Wu, Creating zipper-like van der waals gap discontinuity in low-temperature-processed nanostructured $PbBi_{2n}Te_{1+3n}$: Enhanced phonon scattering and improved thermoelectric performance, Angew. Chem. Int. Ed. 57 (2018) 10938–10943.
[56] B. Xu, M.T. Agne, T. Feng, T.C. Chasapis, X. Ruan, Y. Zhou, H. Zheng, J.H. Bahk, M. G. Kanatzidis, G.J. Snyder, Y. Wu, Nanocomposites from solution-synthesized PbTe-BiSbTe nanoheterostructure with unity figure of merit at low-medium temperatures (500–600 K), Adv. Mater. 29 (2017) 1605140.
[57] F. Tian, B. Song, X. Chen, N.K. Ravichandran, Y. Lv, K. Chen, S. Sullivan, J. Kim, Y. Zhou, T.-H. Liu, M. Goni, Z. Ding, J. Sun, G.A.G.U. Gamage, H. Sun, H. Ziyaee, S. Huyan, L. Deng, J. Zhou, A.J. Schmidt, S. Chen, C.-W. Chu, P.Y. Huang, D. Broido, L. Shi, G. Chen, Z. Ren, Unusual high thermal conductivity in boron arsenide bulk crystals, Science 361 (2018) 582–585.
[58] S. Li, Q. Zheng, Y. Lv, X. Liu, X. Wang, P.Y. Huang, D.G. Cahill, B. Lv, High thermal conductivity in cubic boron arsenide crystals, Science 361 (2018) 579–581.
[59] J.S. Kang, M. Li, H. Wu, H. Nguyen, Y. Hu, Experimental observation of high thermal conductivity in boron arsenide, Science 361 (2018) 575–578.
[60] T. Feng, X. Ruan, Higher-order phonon scattering: advancing the quantum theory of phonon linewidth, thermal conductivity and thermal radiative properties, in: B. Liao (Ed.), Nanoscale Energy Transport, IOP Publishing, 2020, pp. 2–1-2–44, https://doi.org/10.1088/978-0-7503-1738-2ch2.
[61] T. Feng, X. Ruan, Quantum mechanical prediction of four-phonon scattering rates and reduced thermal conductivity of solids, Phys. Rev. B 93 (2016), 045202.
[62] T. Feng, L. Lindsay, X. Ruan, Four-phonon scattering significantly reduces intrinsic thermal conductivity of solids, Phys. Rev. B 96 (2017), 161201.
[63] T. Feng, A. O'Hara, S.T. Pantelides, Quantum prediction of ultra-low thermal conductivity in lithium intercalation materials, Nano Energy 75 (2020), 104916.
[64] T. Feng, X. Ruan, Four-phonon scattering reduces intrinsic thermal conductivity of graphene and the contributions from flexural phonons, Phys. Rev. B 97 (2018), 045202.
[65] Y. Xia, V.I. Hegde, K. Pal, X. Hua, D. Gaines, S. Patel, J. He, M. Aykol, C. Wolverton, High-throughput study of lattice thermal conductivity in binary rocksalt and zinc blende compounds including higher-order anharmonicity, Phys. Rev. X 10 (2020), 041029.
[66] Y. Xia, K. Pal, J. He, V. Ozoliņš, C. Wolverton, Particlelike phonon propagation dominates ultralow lattice thermal conductivity in crystalline Tl_3VSe_4, Phys. Rev. Lett. 124 (2020), 065901.
[67] Y. Xia, V. Ozoliņš, C. Wolverton, Microscopic mechanisms of glasslike lattice thermal transport in cubic $Cu_{12}Sb_4S_{13}$ tetrahedrites, Phys. Rev. Lett. 125 (2020), 085901.
[68] N.K. Ravichandran, D. Broido, Non-monotonic pressure dependence of the thermal conductivity of boron arsenide, Nat. Commun. 10 (2019) 827.
[69] D. Chakraborty, L. de Sousa Oliveira, N. Neophytou, Enhanced phonon boundary scattering at high temperatures in hierarchically disordered nanostructures, J. Electron. Mater. 48 (2019) 1909–1916.
[70] N.N. Greenwood, 13 – Arsenic, antimony and bismuth, in: N.N. Greenwood, A. Earnshaw (Eds.), Chemistry of the Elements, second ed., Butterworth-Heinemann, Oxford, 1997, pp. 547–599. ⟨https://doi.org/10.1016/B978-0-7506-3365-9.50019-5⟩.
[71] C. Hu, K. Xia, C. Fu, X. Zhao, T. Zhu, Carrier grain boundary scattering in thermoelectric materials, Energy Environ. Sci. 15 (2022) 1406–1422.
[72] J.Y.W. Seto, The electrical properties of polycrystalline silicon films, J. Appl. Phys. 46 (1975) 5247–5254.
[73] J. Yang, L. Yu, T. Wang, J. Yan, G. Liu, Z. Shi, G. Qiao, Thermoelectric properties of n-type $Cu_xBi_2S_3$ materials fabricated by plasma activated sintering, J. Alloy. Compd. 780 (2019) 35–40.
[74] L. Ai, D. Jia, N. Guo, M. Xu, S. Zhang, L. Wang, L. Jia, Cl-doped Bi_2S_3 homojunction nanorods with rich-defects for collaboratively boosting photocatalytic reduction performance, Appl. Surf. Sci. 529 (2020), 147002.
[75] Y. Cheng, Y. Chang, Y. Feng, H. Jian, Z. Tang, H. Zhang, Deep-level defect enhanced photothermal performance of bismuth sulfide-gold heterojunction

nanorods for photothermal therapy of cancer guided by computed tomography imaging, Angew. Chem. Int. Ed. Engl. 57 (2018) 246–251.
[76] R. Chmielowski, D. Péré, C. Bera, I. Opahle, W. Xie, S. Jacob, F. Capet, P. Roussel, A. Weidenkaff, G.K.H. Madsen, G. Dennler, Theoretical and experimental investigations of the thermoelectric properties of Bi_2S_3, J. Appl. Phys. 117 (2015), 125103.
[77] D. Han, M.-H. Du, C.-M. Dai, D. Sun, S. Chen, Influence of defects and dopants on the photovoltaic performance of Bi_2S_3: first-principles insights, J. Mater. Chem. A 5 (2017) 6200–6210.
[78] K. Lejaeghere, V. Van Speybroeck, G. Van Oost, S. Cottenier, Error estimates for solid-state density-functional theory predictions: an overview by means of the ground-state elemental crystals, Crit. Rev. Solid State Mater. Sci. 39 (2014) 1–24.
[79] J.P. Perdew, M. Levy, Physical content of the exact Kohn-Sham orbital energies: band gaps and derivative discontinuities, Phys. Rev. Lett. 51 (1983) 1884–1887.
[80] J. Yan, J. Yang, B. Ge, G. Liu, Z. Shi, Z. Duan, G. Qiao, Effect of silver and iodine co-doping on the thermoelectric properties of n-type Bi_2S_3, J. Electron. Mater. 48 (2018) 503–508.

Kangpeng Jin is a Ph.D. Candidate with Prof. Biao Xu in School of Chemistry and Chemical Engineering at Nanjing University of Science and Technology. His current research interests are mainly focused on the chemical synthesis of high-performance thermoelectric materials, together with DFT calculation.

Janak Tiwari is a Ph.D. Candidate in Dr. Tianli Feng's group in the Department of Mechanical Engineering at the University of Utah. His research includes atomistic phonon, electron, and photon thermal transport simulations and finite-element heat transfer simulations. He received his M.S. degree from the University of Mississippi, 2021.

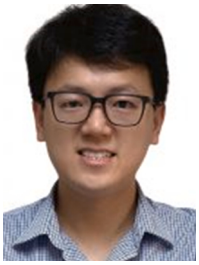

Tianli Feng is an assistant professor of the Department of Mechanical Engineering at the University of Utah. He was an R&D Associate Staff Scientist at Oak Ridge National Laboratory before 2021. He received his M.S. and Ph.D. degrees from the School of Mechanical Engineering at Purdue University. He received his B.S. degree in Physics from the University of Science and Technology of China (USTC). His research covers atomic-to-large scale simulations of thermal, electrical, and structural properties of various materials.

Yue Lou received her Ph.D. degree from the State Key Laboratory of Inorganic Synthesis and Preparative Chemistry, College of Chemistry, Jilin University in 2020. Then she joined in Nanjing University of Science and Technology as a lecturer until now. Her research interests focus on the synthesis of metal chalcogenides-based energy materials and their applications in thermoelectric, photoelectric, and lithium-ion batteries.

Biao Xu was born in Zhenjiang, Jiangsu, in July 1987. He obtained his bachelor and Ph.D. degrees in 2009 and 2014 from Tsinghua University, under the supervision of Prof. Xun Wang. Then he carried out postdoctoral research under the supervision of Prof. Yue Wu, in Iowa State University, USA. He was appointed as a full professor of Nanjing University of Science and Technology in 2018, and elected as '1000 National Young Talents from Overseas' in 2019. His research interests include the syntheses, characterization and theoretical analyses of thermoelectric materials.

Supporting Information for

Realizing high thermoelectric performance in eco-friendly Bi_2S_3 with nanopores and Cl-doping through shape-controlled nano precursors

Kangpeng Jin [a], Janak Tiwari [b], Tianli Feng [b,*], Yue Lou [a,*], Biao Xu [a,*]

[a] School of Chemistry and Chemical Engineering, Nanjing University of Science and Technology, Nanjing, 210094, China;

[b] Department of Mechanical Engineering, The University of Utah, Salt Lake City, UT 84112, USA.

*** Corresponding Authors:**
tianli.feng@utah.edu (Tianli Feng)
louyue@njust.edu.cn (Yue Lou)
xubiao@njust.edu.cn (Biao Xu)

Contents:

Table S4. The related parameters to estimate α_{BD} for Cl-doped Bi_2S_3.

Supplementary Note 1: Flask synthesis of FL-NN and FL-NR.

Supplementary Note 2: Characterization methods.

Supplementary Note 3: Lotgering factor estimation for bulk samples.

Supplementary Note 4: The reason why HT-NN has almost no bipolar thermal conductivity.

Supplementary Note 5: The calculation of electronic polar Lorenz number (L_1) and density of states effective mass (m^*) via single parabolic band (SPB) model.

Supplementary Note 6: The fit of bipolar thermal conductivity for HT-NR.

Supplementary Note 7: First-principles calculation details.

Supplementary Note 8: BTE modeling of lattice thermal conductivity.

Supplementary Note 9: Determining the dominant scattering mechanism by a dimensionless parameter α_{BD} when μ increases exponentially with temperature.

Supplementary Note 10.: The energy gap of Bi_2S_3 in high temperatures.

Supplemental References.

Supplementary Figures

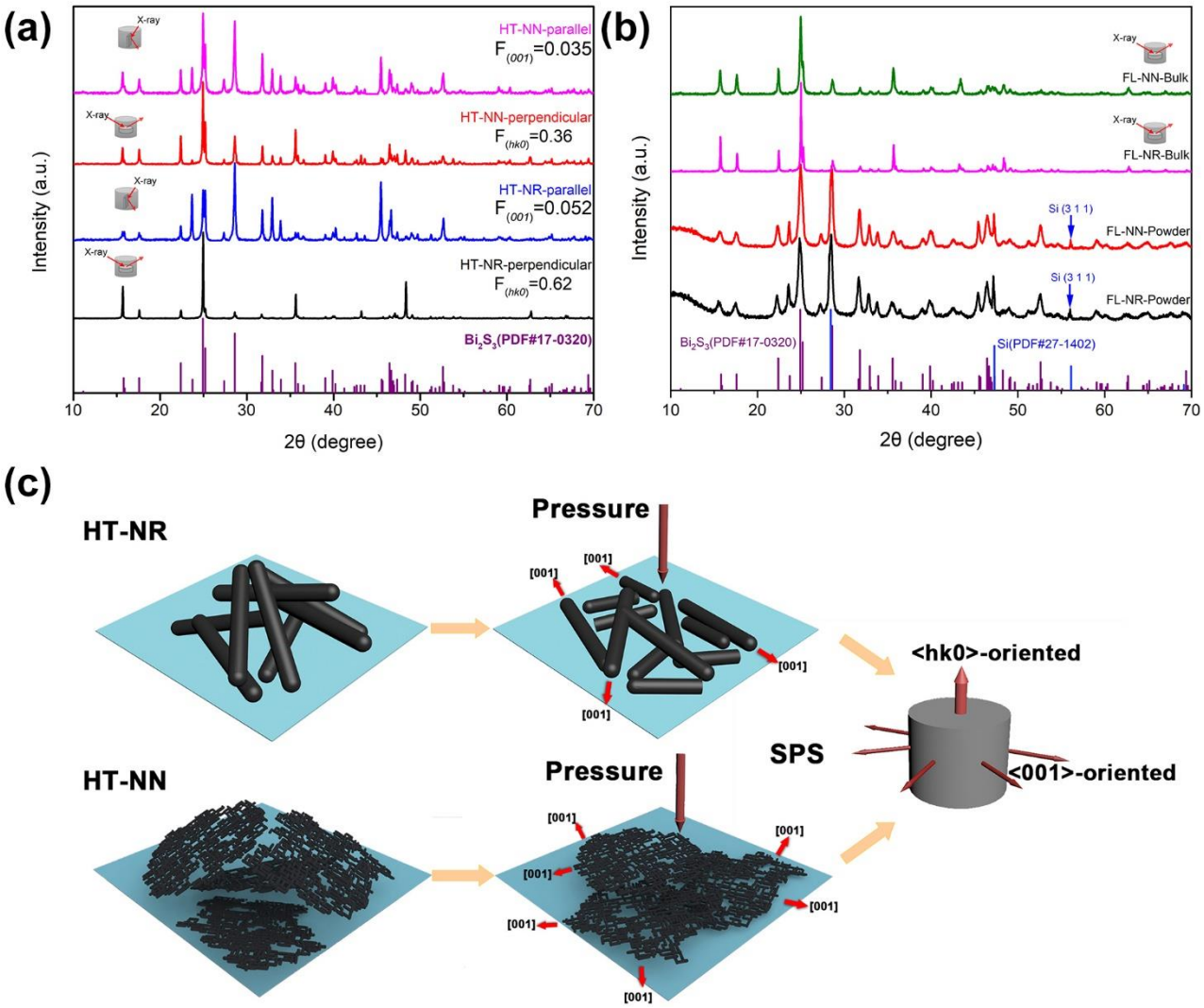

Fig. S1. XRD patterns of (a) sintered samples of HT-NN and HT-NR. Silicon powder is used as an internal standard for powder samples. The inset shows that the measurement is perpendicular or parallel to the sintering pressure direction with corresponding Lotgering factors, showing obvious anisotropy, (b) powder and sintered sample of FL-NN and FL-NR, (c) schematic diagram of the formation mechanism of preferred orientation.

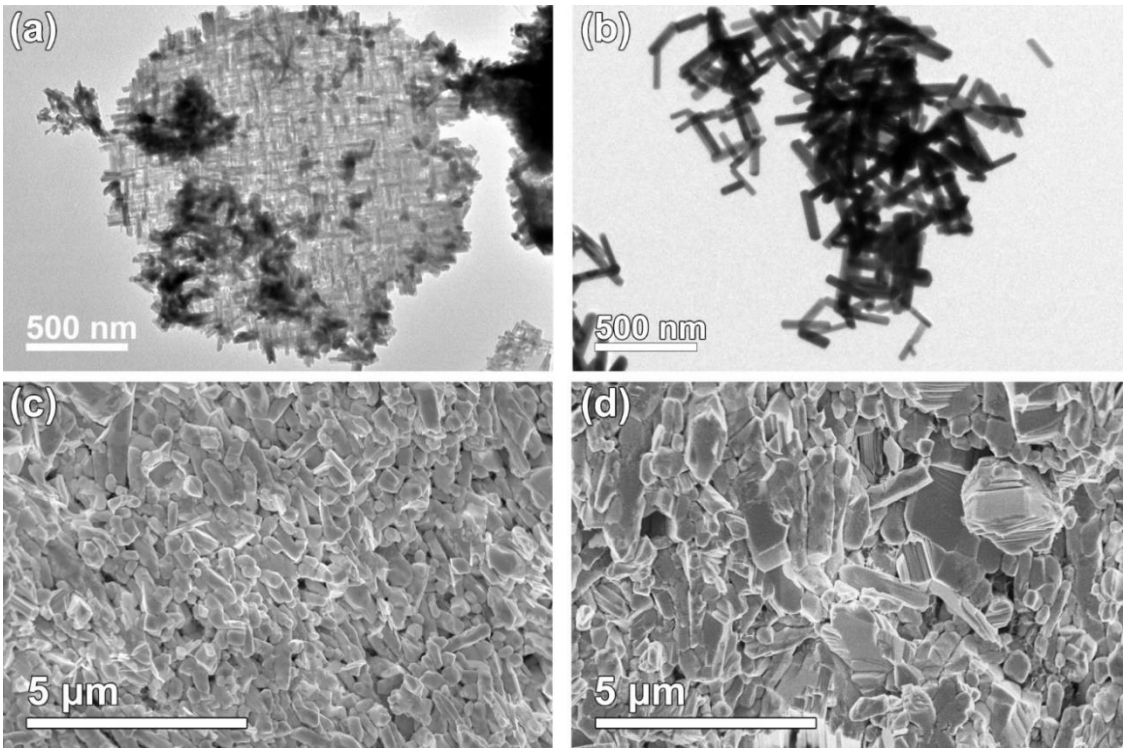

Fig. S2. The low-magnification TEM image of (a) FL-NN and (b) FL-NR. The SEM image of fractures of (c) FL-NN and (d) FL-NR. Similar to the samples prepared by hydrothermal method (HT-NN and HT-NR), the sizes of nanorods of the two samples are similar, but the morphologies are different, which makes the grain size and porosity of the sintered samples different. The average density of FL-NN is 5.70 ± 0.14 g·cm^{-3}, while that of FL-NR is 6.14 ± 0.09 g·cm^{-3}.

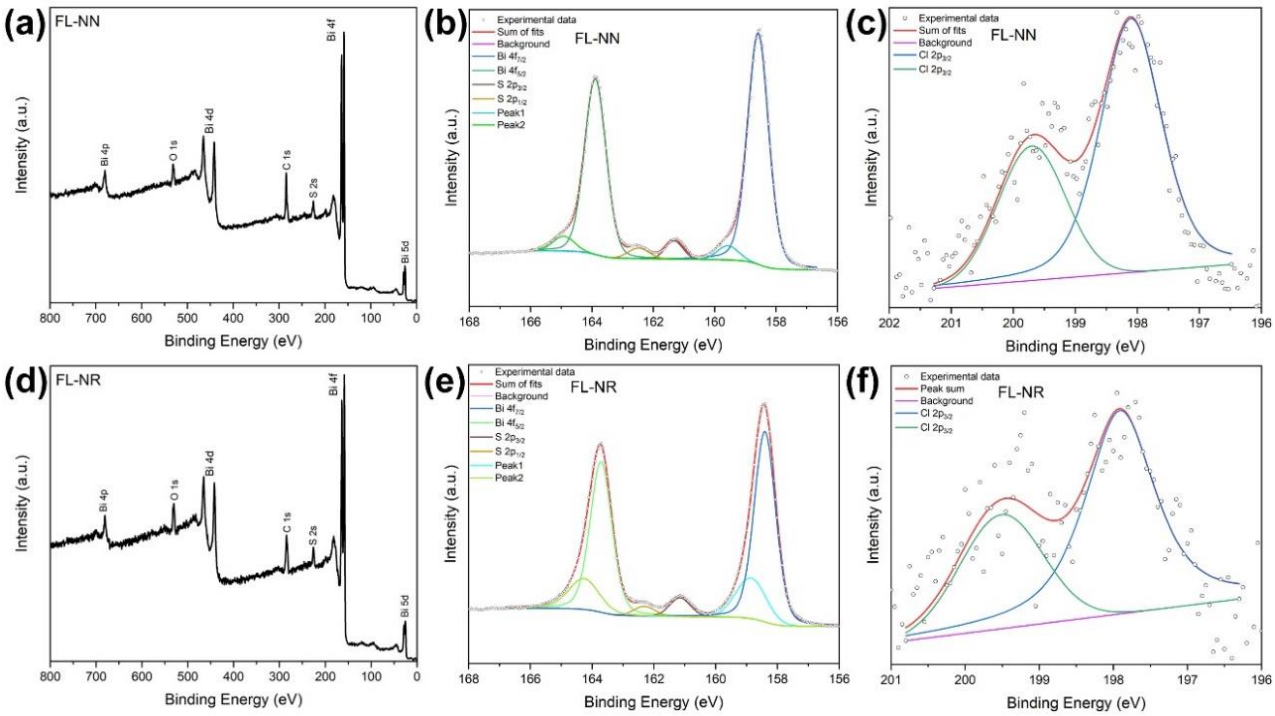

Fig. S3. XPS spectra of fractured surfaces of FL-NN and FL-NR. (a) the survey spectra of FL-NN; (b) the peak fitting of Bi 4f in FL-NN; (c) the peak fitting of Cl 2p in FL-NN; (d) the survey spectra of FL-NR; (e) the peak fitting of Bi 4f in FL-NR; (f) the peak fitting of Cl 2p in FL-NR. These results are similar to those of HT-NN and HT-NR (Fig.7 a-b), indicating that Cl was successfully doped into Bi_2S_3 lattice.

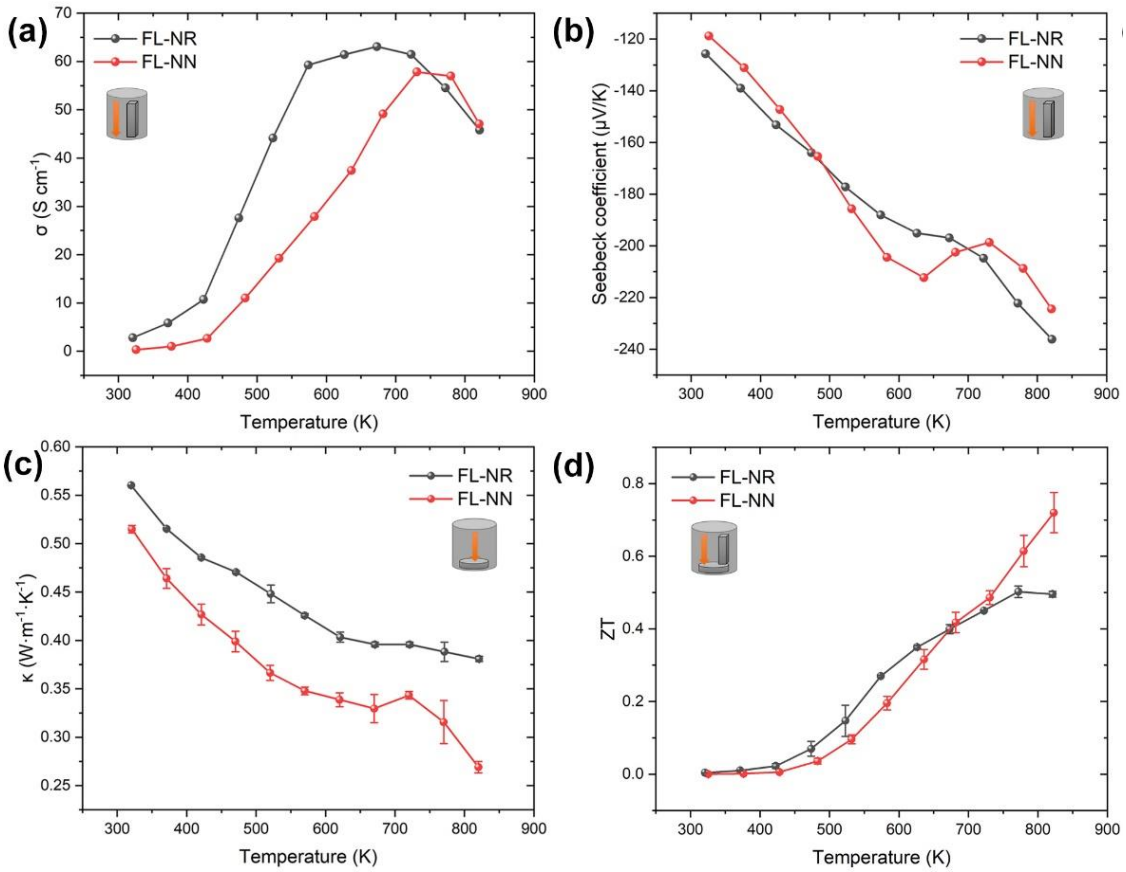

Fig. S4. Temperature-dependent thermoelectric properties of FL-NN and FL-NR in the direction parallel to the sintering pressure: (a) Electrical conductivity, (b) Seebeck coefficient, (c) thermal conductivity, and (d) figure of merit. The electrical properties and thermal conductivity of FL-NN and FL-NR were averaged from the data of three batches of samples. The thermal conductivities are calculated through $\kappa = C_p \cdot \rho \cdot D$, where C_p is Dulong-Petit limit (0.24255 J g^{-1} K^{-1}).

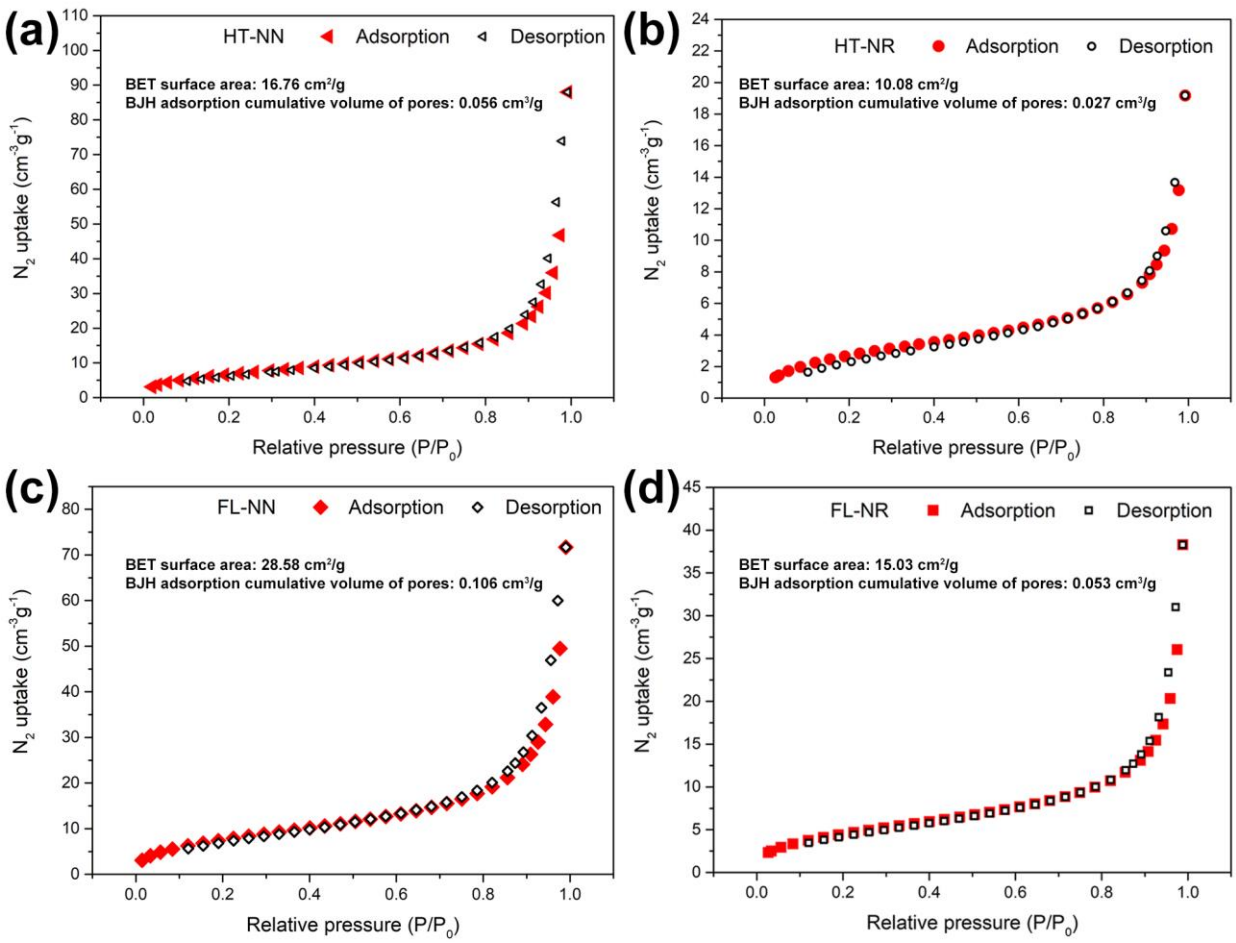

Fig. S5. The isothermal adsorption and desorption curves of (a) HT-NN, (b) HT-NR, (c) FL-NN, and (d) FL-NR measured at 77 K. The related fitting data through BET and BJH equation are listed in the figure.

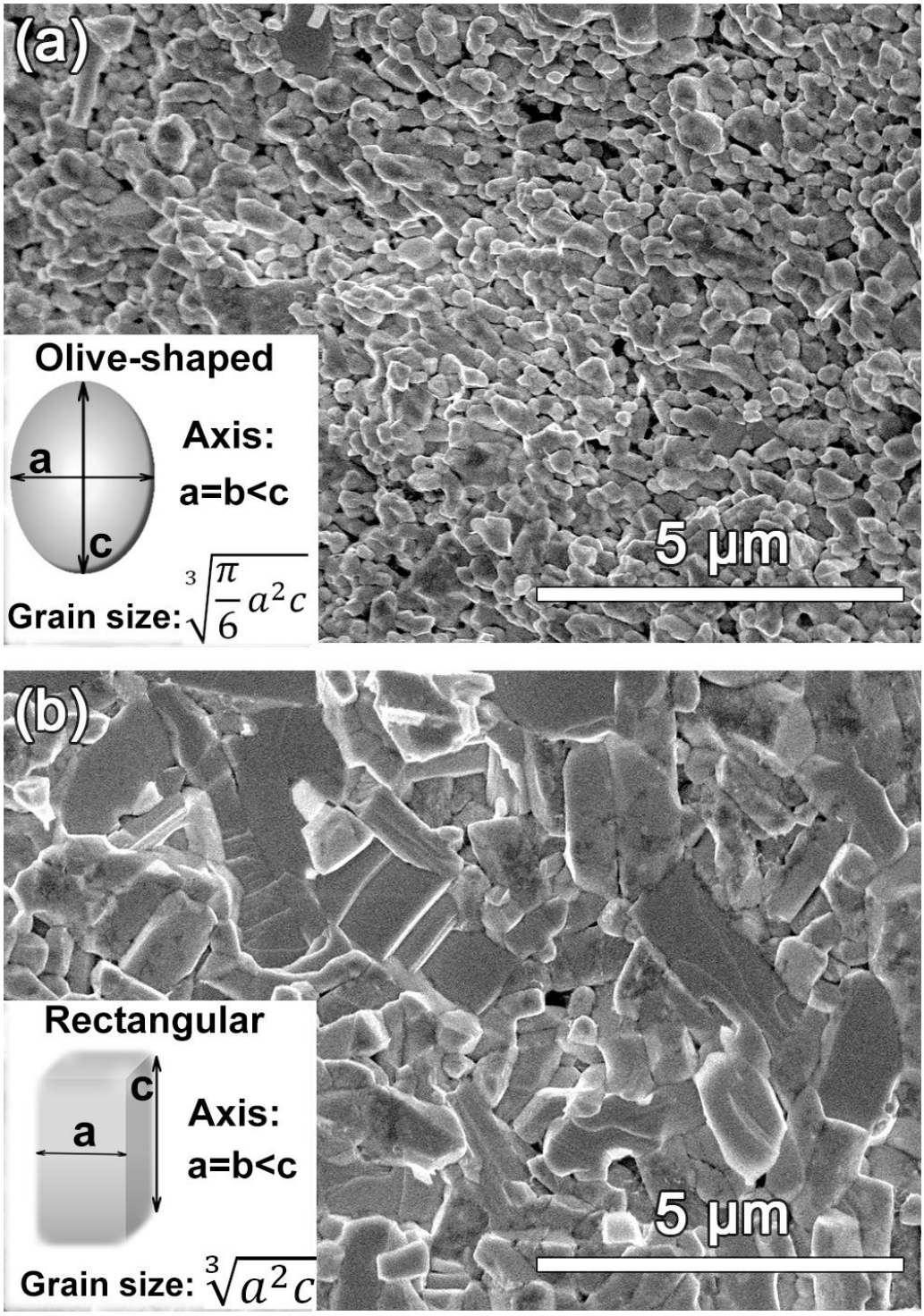

Fig. S6. The low-magnification SEM image of fractured surfaces of (a) HT-NN and (b) HT-NR. We made statistics on the long and short axes of individual grains (assuming the length of the two short axes is equal) and the side length of the cubes with the same grain volume is taken as the final size of single grain (**Scheme inset**). Five SEM images (11 μm in length and 7 μm in width) of fractured surfaces in different regions were used as statistics for each sample, and the size data of more than 1000 grains were made into the frequency histograms (Fig. 3c inset), which were better matched by fitting the Gauss distribution function.

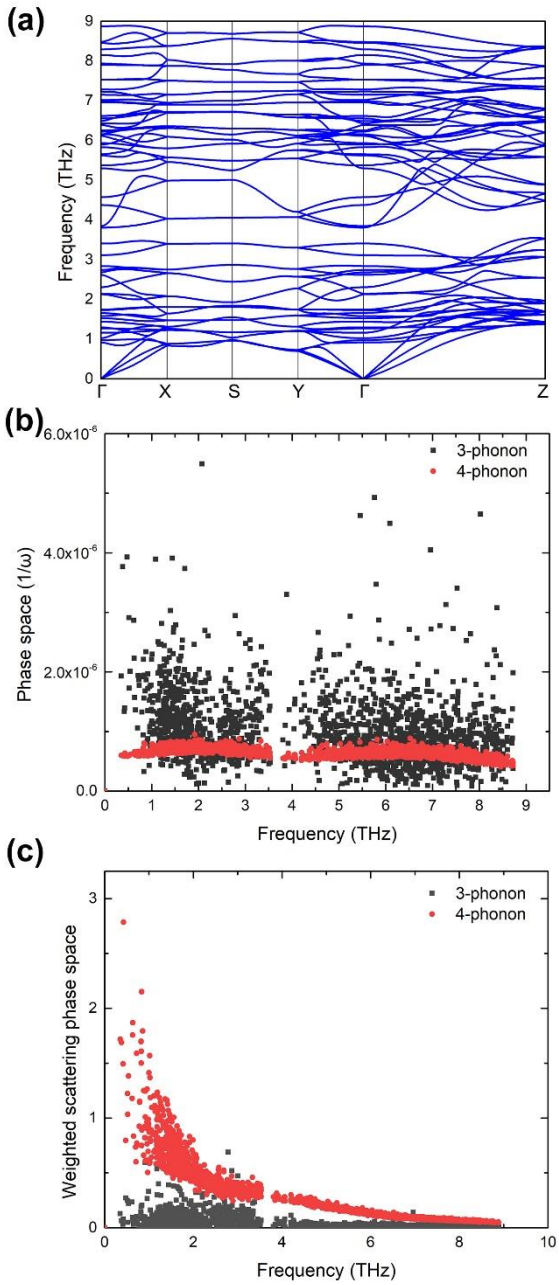

Figure S7. (a) First-principles phonon dispersion relation curve for orthorhombic Bi_2S_3; (b) scattering phase space for 3-phonon and 4-phonon; (c) weighted scattering phase space for 3-phonon and 4-phonon.

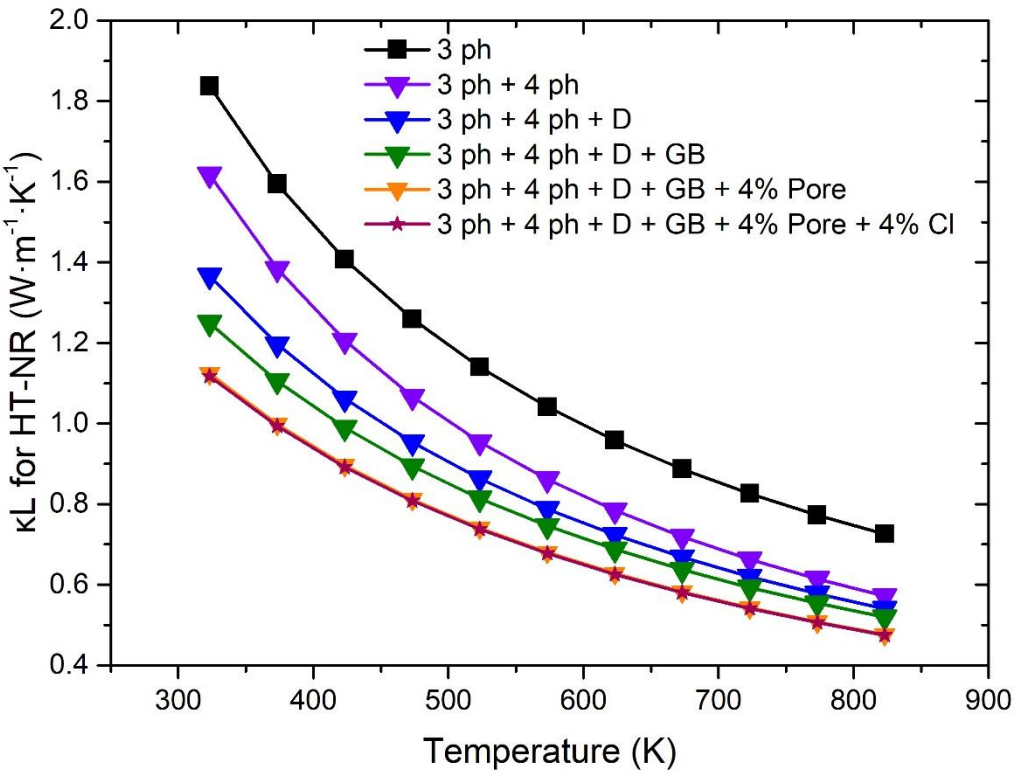

Figure S8. Drop of κ_L due to various phonon scattering mechanisms in HT-NR. (Umklapp process of three-phonon (*3-ph*) and four-phonon (*4-ph*), defects (*D*), grain boundaries (*GB*), pores in the nanoscale (*Pore*), and chlorine doping (*Cl*)).

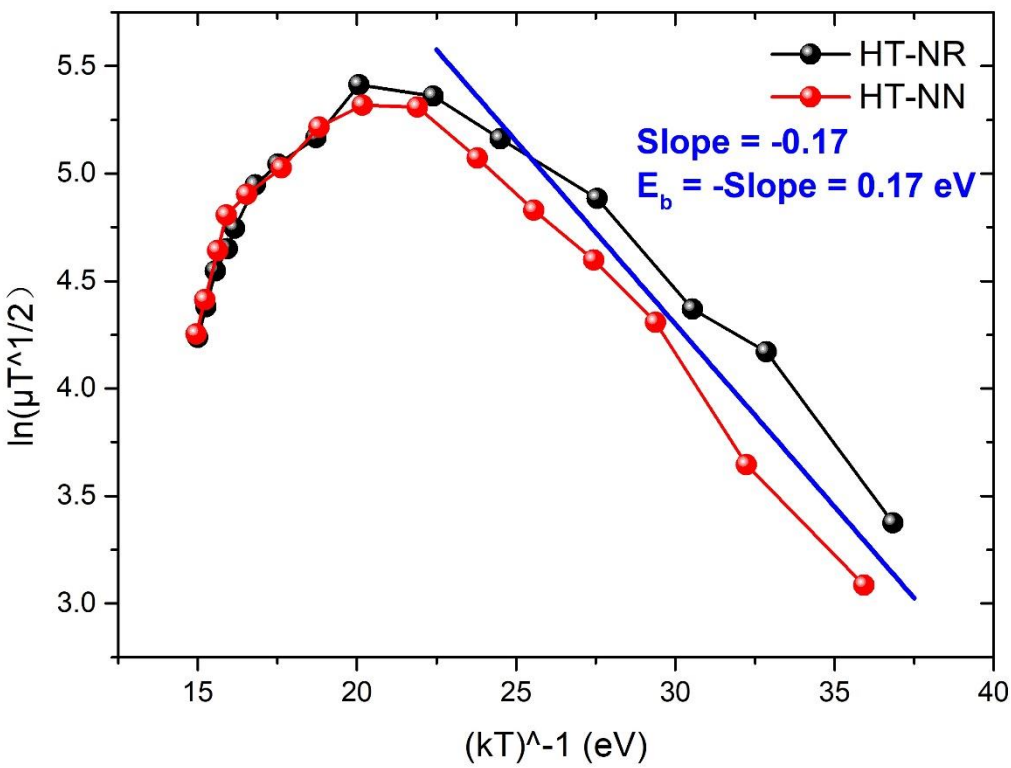

Figure S9. The linear fit of grain boundary potential barrier (E_b).

The carrier mobility can be simulated from the equation proposed by Seto [1]

$$\mu = ed\left(\frac{1}{2\pi m^* k_B T}\right)^{1/2}\exp\left(\frac{-E_b}{k_B T}\right). \quad (1)$$

The energy barrier E_b can be obtained from the slope of $\ln(\mu T^{1/2})$ - $(kT)^{-1}$ curve for both HT-NR and HT-NN when the temperature is low (300–500 K).

$$\ln\left(\mu T^{\frac{1}{2}}\right) = -\frac{E_b}{kT} + C. \quad (2)$$

The E_b values for both HT-NR and HT-NN are about 170 meV. The large value of E_b is in the reasonable range (for instance: 73 meV in PbSe [2]; 60 meV in PbTe [3]; 169 meV in SnSe [4]).

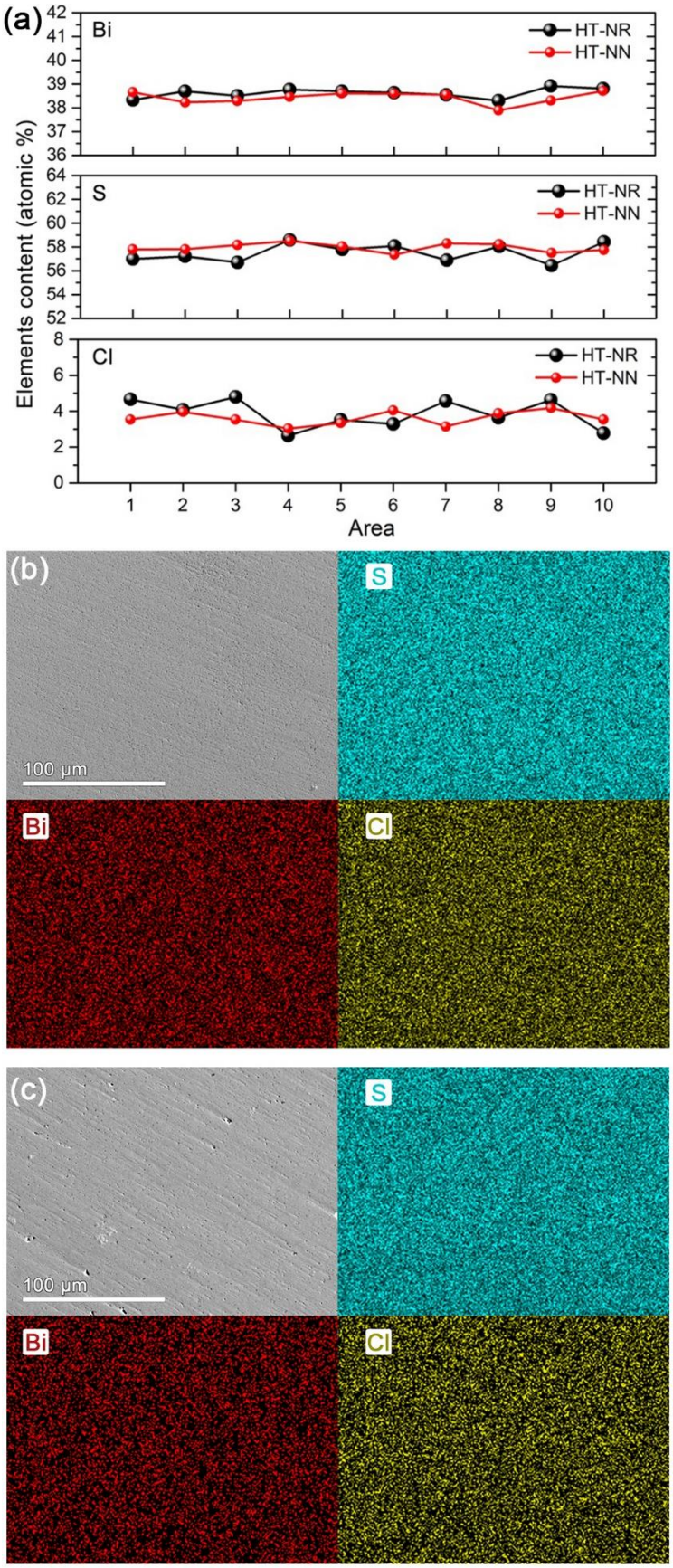

Fig. S10. (a) Element content based on EPMA measurement. EPMA elemental mapping of (b) HT-NN and (c) HT-NR.

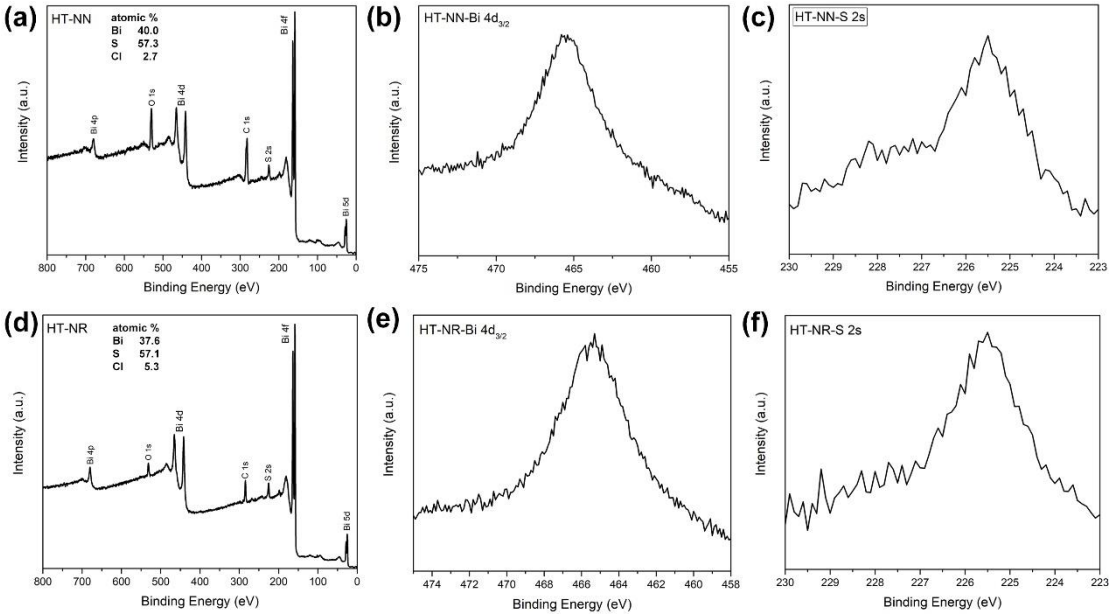

Fig. S11. The XPS survey spectra of (a) HT-NN and (d) HT-NR. The peak areas of Bi $4d_{3/2}$, S 2s, and Cl 2p are selected for semi-quantitative analysis, which reveals that Cl contents are 5.3 atomic% and 2.7 atomic% for HT-NN and HT-NR after sintering respectively, which are close to EPMA quantitative analysis.

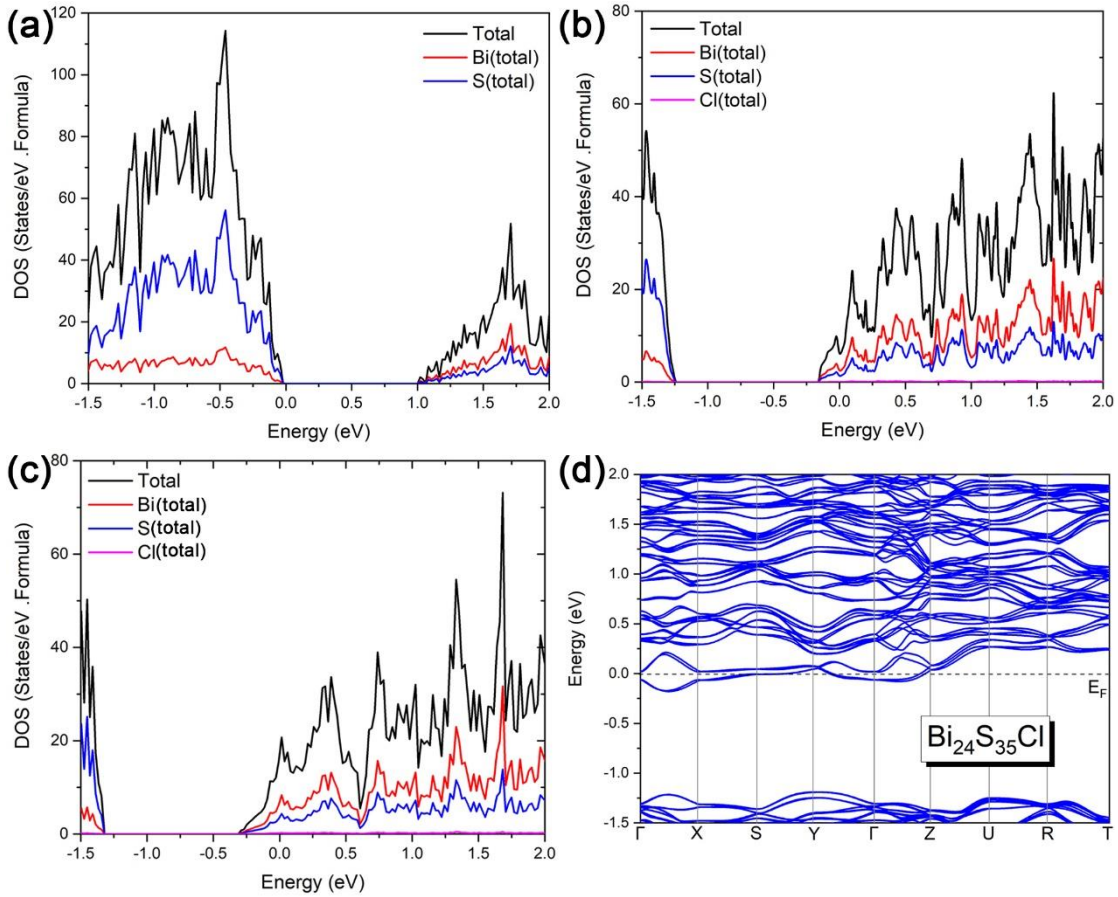

Fig. S12. The electronic density of states (DOS) of (a) pristine Bi_2S_3 (supercell $Bi_{24}S_{36}$), (b) 1.7 % Cl-doped Bi_2S_3 ($Bi_{24}S_{35}Cl$), and (c) 3.3 % Cl-doped Bi_2S_3 ($Bi_{24}S_{34}Cl_2$). (d) Band structure of 1.7 % Cl-doped Bi_2S_3 ($Bi_{24}S_{35}Cl$). E=0 labels the valence band maximum for pristine Bi_2S_3 and Fermi level for doped Bi_2S_3.

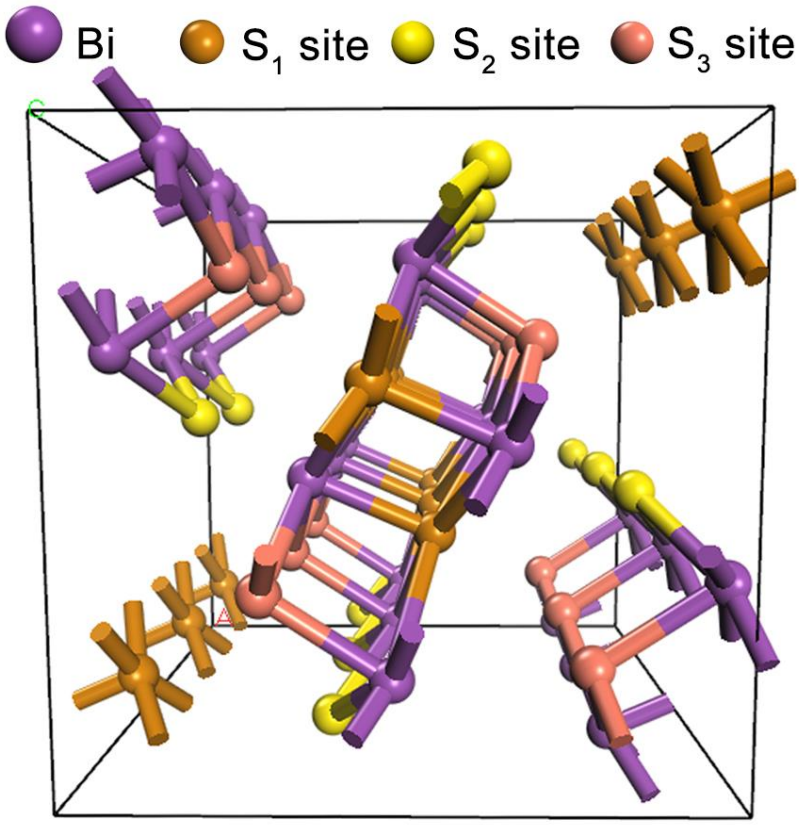

Fig. S13. The perspective view of Bi_2S_3 supercell in the direction of [0 0 1] zone axis. Sulfur sites in three different chemical environments are distinguished.

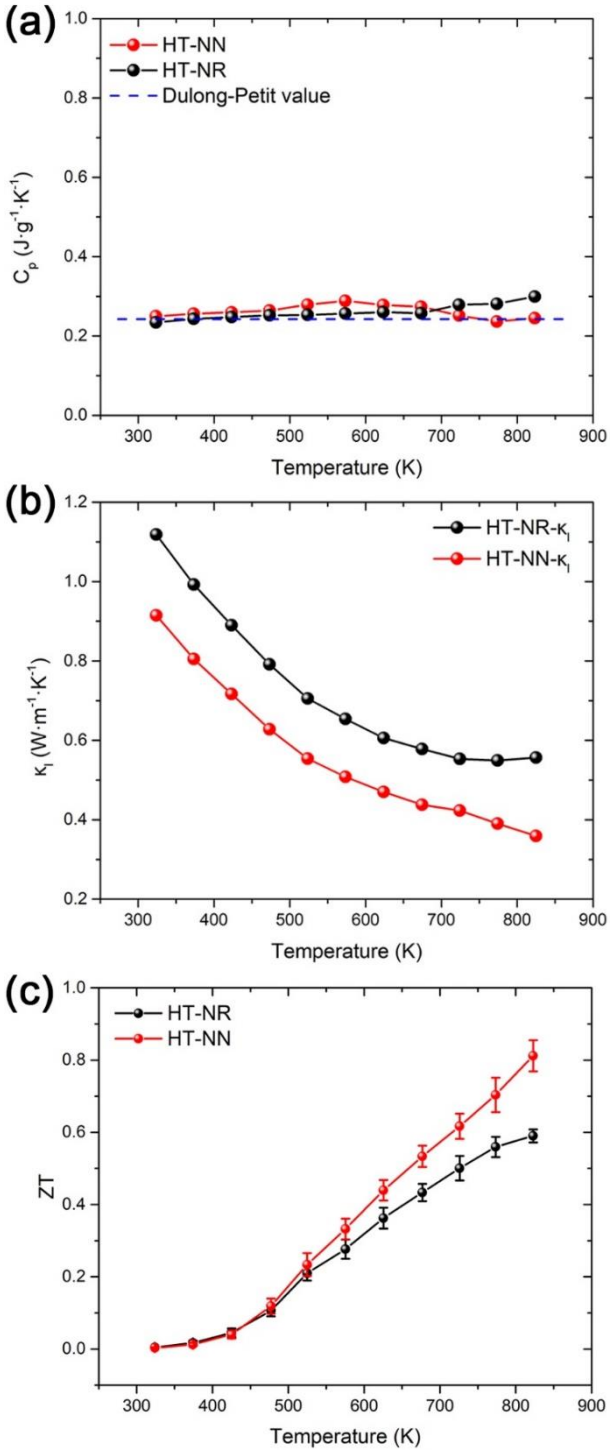

Fig. S14. (a) Specific heat at constant pressure (C_p) of HT-NN and HT-NR; (b) thermal conductivity of HT-NN and HT-NR calculated through Dulong-Petit limit (C_p = 0.24255 J·g^{-1}·K^{-1}); (c) ZT values of HT-NN and HT-NR calculated through Dulong-Petit limit. The highest ZT value of HT-NN is also 0.81, which is 35 % higher than that of HT-NR (0.59).

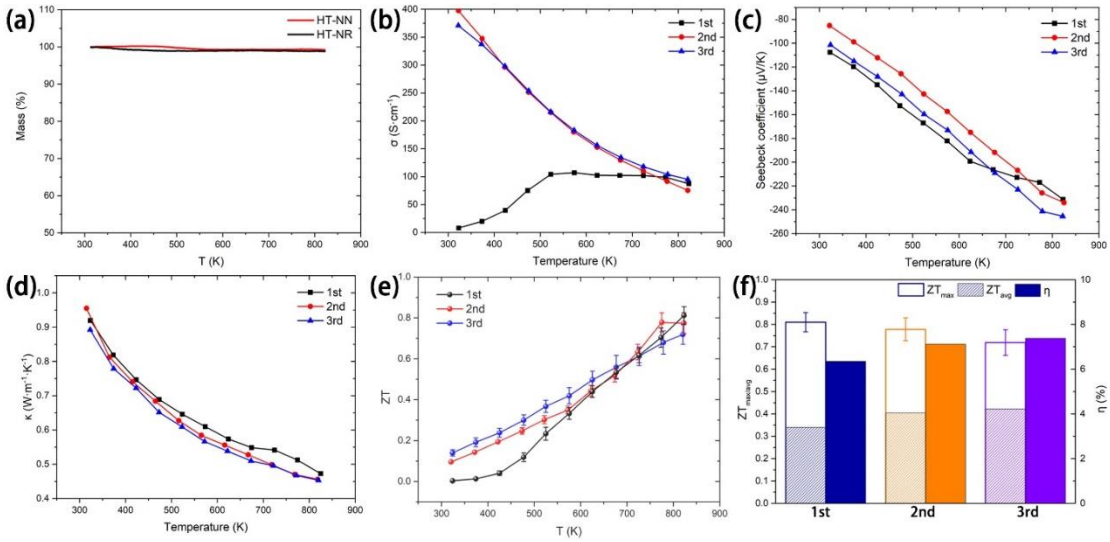

Fig. S15. (a) Thermogravimetric analysis (TGA) of HT-NN and HT-NR. The weight losses of both samples are less than 1%. Temperature-dependent thermoelectric properties in cycle test of HT-NN: (b) electric conductivity, (c) Seebeck coefficient, (d) thermal conductivity, and (e) *ZT* values. (f) the maximum *ZT*, average *ZT*, and conversion efficiency of three cycles of measurement. All results of cycle test were averaged from the data of three different samples under three heating processes (1st, 2nd, and 3rd), and the relative error is displayed as error bars in *ZT* values (Fig. S10e). Although the maximum *ZT* value decreases during the cyclic test, the average *ZT* increases due to the significant increase in electric conductivity, resulting in a theoretical conversion rate of 7.3%, which is the highest value in Bi_2S_3 system.

Supplementary Tables

Table S1. The cell parameter of powder and SPSed bulk sample from Rietveld refinement data.

Sample	a (Å)	b (Å)	c (Å)
FL-NN-Powder	11.16819	11.29359	3.98703
FL-NR-Powder	11.17555	11.33123	3.98961
FL-NN-Bulk	11.14772	11.28284	3.97763
FL-NR-Bulk	11.13694	11.27924	3.98215
HT-NN-Powder	11.17493	11.31055	3.99054
HT-NR-Powder	11.17982	11.30584	3.99164
HT-NN-Bulk	11.14534	11.27898	3.98441
HT-NN-Bulk	11.12678	11.26615	3.98004

Table S2. Lattice parameter, total energy, Fermi level and defect formation energy for pristine and Cl-doped Bi_2S_3 through DFT calculation. The chemical potentials of S (μ_S) and Cl (μ_{Cl}) are -4.127 eV and -1.787 eV, respectively.

Supercell component	Lattice parameter (Å)			Total energy (eV)	Fermi level (eV)	Formation energy (eV)
	a	b	c (3X supercell)			
$Bi_{24}S_{36}$	11.167	11.791	12.051	-262.66	4.020	N/A
$Bi_{24}S_{35}Cl$ (replace S_1)	11.175	11.780	12.071	-260.46	5.584	-0.14
$Bi_{24}S_{35}Cl$ (replace S_2)	11.161	11.746	12.148	-260.63	5.632	-0.31
$Bi_{24}S_{35}Cl$ (replace S_3)	11.165	11.753	12.151	-260.65	5.598	-0.33
$Bi_{24}S_{34}Cl_2$ (replace S_3)	11.163	11.709	12.193	-258.52	6.167	-0.54
$Bi_{24}S_{36}Cl$ (interstitially doping)	11.106	12.408	12.081	-263.62	3.673	0.83
$Bi_{24}S_{36}Cl_2$ (interstitially doping)	12.240	12.800	12.125	-265.56	3.473	0.67

Supplementary Note 1:

Flask synthesis of FL-NN and FL-NR

Synthesis of Bi_2S_3 nanorod network via flask (FL-NN): 6.25 mL dilute HCl solution (3 M) that contained 2.5 mmol $BiCl_3$ was added in 250 ml ultrapure water with stirring. Then, 25 mL TAA (12.5 mmol) solution was added slowly in this white suspension. Before the reaction starts, high purity nitrogen is pumped for 5 minutes to exhaust as much oxygen as possible and seal the reaction unit. In the open reaction system, by-product S is generated, which is attributed to the side reaction caused by long-term contact between oxygen and excess hydrogen sulfide. The reaction temperature was kept at 60 °C for 72 hours. Bi_2S_3 black powder was obtained and washed 3 times with water and ethanol separately. The sediment was dried at 60 °C in vacuum for 6 hours.

Synthesis of Bi_2S_3 disordered nanorod via flask (FL-NR): 3.648 g $BiCl_3$ (11.6 mmol) and 3 mL HCl (12 M) were successively added to 250 mL deionized water. After stirring, 3.93 g TAA (52.35 mmol) was added, and the solution changed from milky white to brownish-yellow. Then, the mixture was incubated at 60 °C with stirring for 72 hours. The washing and drying procedures of the product were the same as those of FL-NN.

The sintering procedures are the same as those of HT-NN and HT-NR samples. The thermoelectric performance parallel to the pressure direction is optimal. The sintered bulk was cut into 3 mm*3 mm*10 mm cuboid ingot and Φ10 mm*1.5 mm disc to measure its electrical and thermal performance, respectively.

Supplementary Note 2:

Characterization methods

The crystal information of two types of as-synthesized powders was identified via powder X-ray diffraction (XRD, AXS D8 Advance, Bruker) with monochromatic Cu-Kα radiation. The thermogravimetric analysis (TGA, STA449F3, NETZSCH) of bulk samples was performed from 323 K to 873 K with a heating rate of 10 K/min. Nitrogen adsorption and desorption isotherms were measured on a specific surface area and porosity analyzer (Asap2020, Micromeritics) at 77 K. The morphology of two powder samples was investigated via transmission electron microscope (TEM, TECNAI G2 20 LaB_6, FEI) and scanning electron microscope (SEM, JSM-IT500HR, JEOL). The fractography of sintered specimens was also characterized by scanning electron microscopy (SEM, JSM-IT500HR, JEOL). The spherical aberration correction TEM (Cs-TEM, Titan G2 60-300, FEI) was utilized to analyze the lattice image of the bulk sample. The bulk sample for Cs-TEM testing was prepared by the ion thinning technique (Gatan 695C, Gatan). Ar ions were used to thin out the small holes at 8° and trim the edge area at 4° with a voltage of 5 kV. The composition of elements and the chemical states of elements contained in the samples were analyzed by X-ray Photoelectron Spectroscopy (XPS, Thermo Scientific K-alpha, Thermo Field Company) using Al-Kα micro-focusing monochromatic X-ray source (1486.6 eV). C 1s peak (284.8 eV) was used to calibrate peak positions. The Electron Probe Micro-analyzer (EPMA, JXA-8230, JEOL) was used to characterize the element content and distribution in bulk samples. The synchrotron radiation small-angle X-ray scattering (SAXS) measurements were conducted at Shanghai Synchrotron Radiation Facility (SSRF, Shanghai, China) SAXS beamline (BL19U2). Bi_2S_3 bulk samples were polished into slides with a thickness of 0.15 mm to avoid multiple scattering effects during testing. The wavelength of the X-ray was 1.033 Å, and the distance from the sample to the detector was 2190 mm. The scattering model was collected by a detector (Pilatus 2M, DECTRIS) with a pixel size of 172 μm × 172 μm.

Supplementary Note 3:

Lotgering factor estimation for bulk samples

Comparing the diffraction peaks of the same bulk sample in different directions, it is found that all the diffraction peaks of crystal planes parallel to the c-axis ({h k 0}, where h and k are co-prime) in the direction perpendicular to sintering pressure are enhanced. For bulk's surface in the SPS pressure direction, the diffraction peaks of (0 0 1) crystal plane are stronger (**Figure S1a**). The reason for this phenomenon is illustrated in **Figure S1c**. In HT-NN precursors, the huge pressure causes the nanodiscs to pile up horizontally. The vertical or tilted nanodiscs are crushed and further flattened to horizontal. Since the single nanorod is <0 0 1>-oriented in plane, the sintered bulk is <h k 0>-oriented in the cleavage surface under press direction after SPS process. The SPS process of HT-NR is similar.

The Lotgering factor is a quality factor to characterize the degree of preferred orientation in given samples [5]:

$$\begin{cases} F_{(hk0)} = \frac{p-p_0}{1-p_0} \\ p = \frac{\sum I(hk0)}{\sum I} \end{cases}, \quad (1)$$

where $F_{(hk0)}$ is the Lotgering factor of particular crystal planes (h k 0), p or p_0 is a ratio of sum intensities of (h k 0) plane and all the diffraction peaks in a certain 2θ range (15-50°) from given material or JCPDS data of Bi_2S_3, respectively. For materials with random orientation, its Lotgering factor is 0. The Lotgering factor of 1 means a perfectly textured material.

The calculated Lotgering factors are listed in **Table 1**, reflecting obvious anisotropy.

Supplementary Note 4:

The reason why HT-NN has almost no bipolar thermal conductivity

According to the bipolar effect, the bipolar thermal conductivity can be divided into the contribution of majority carrier conductivity and minority carrier conductivity, as shown in the following equations [6]:

$$\kappa_b = \frac{\sigma_n \sigma_p}{\sigma_n + \sigma_p}(S_n - S_p)^2 T, \quad (2)$$

where the κ_b is bipolar thermal conductivity, the subscript n denotes electrons as carriers, and subscript p denotes holes as carriers.

The obvious bipolar thermal conductivity of HT-NR may be caused by the difference of minority carriers (σ_p) between the two.

The contribution of minority carriers to conductivity can be expressed as follows [6]

$$\sigma_p = \frac{pe^2\tau_p}{m_p^*}, \quad (3)$$

where p is hole concentration, τ_p is hole relaxation time, and m_p^* is hole effective mass, respectively.

In semiconductors, the product of electron and hole concentration can be expressed as a function independent of the Fermi level [7]:

$$np = N_C N_V \exp(-\frac{E_g}{kT}), \quad (4)$$

where N_C and N_V are effective densities of states in the conduction and valence band respectively, and E_g is the band gap. The N_C and N_V are both the function of carrier effective mass and temperature. DFT calculation results also show that the change of chlorine doping amount does not affect the band gap and the band shape of valence band maximum or conduction band minimum. Therefore, the p and m_p^* of both can be regarded as not changing much. Considering that the majority carrier concentration (n) is also close, the only difference between the two is mainly reflected in the difference of relaxation time of the minority carrier (τ_p).

It can be seen from the information in **Table S3** below that HT-NN has more abundant nanostructures. Some theoretical and experimental reports have demonstrated that the nanostructure can inhibit the bipolar effect [8, 9]. We can qualitatively hypothesize that HT-NN's refined grains, nanoscale pores, and appropriately high porosity enhanced its scattering factor, resulting in a smaller τ_p. The mean free path of the hole is relatively shorter [9], so it is easily scattered by these nanostructures. As a result, the contribution of minority carriers is smaller in HT-NN, and its bipolar

effect is less obvious. Besides, the difference of minority carriers has a slight effect on electrical conductivity and Seebeck coefficient. For HT-NN, the stronger scattering of minority carriers causes the electrical conductivity to decrease rather than increase in the intrinsic excitation region, and the Seebeck coefficient is still increasing gradually, which is consistent with the experimental results (**Figure 6**).

Table S3. The nanostructure comparison of HT-NR and HT-NN.

Samples	Doping concentration from EPMA	Grain size from SEM	Pore size from SAXS	Porosity from relative density
HT-NR	3.67 % Cl	620 nm	77 nm	4.7%
HT-NN	3.47 % Cl	190 nm	37 nm	11.0%

Supplementary Note 5:

The calculation of electronic polar Lorenz number (L_1) and density of states effective mass (m^*_{DOS}) via single parabolic band (SPB) model

In the case of electron scattering by the acoustical vibrations of the lattice atoms, the Lorenz number contributed by polar electrons can be expressed as [10]

$$L_1 = (\frac{k_B}{e})^2 \frac{3F_0(\eta)F_2(\eta)-4F_1^2(\eta)}{F_0^2(\eta)}. \quad (5)$$

And the reduced Fermi level η can be obtained from the measured Seebeck coefficient through the following equations:

$$S = -\frac{k_B}{e}[2\frac{F_1(\eta)}{F_0(\eta)} - \eta] \quad (6)$$

$$F_n(\eta) = \int_0^\infty \frac{\chi^n}{1+e^{\chi-\eta}} d\chi. \quad (7)$$

$F_n(\eta)$ is the nth Fermi integral, and k_B is the Boltzmann constant. The density of states effective mass can be fitted from experimental Seebeck coefficient, as shown in the following equations:

$$m^*_{DOS} = \frac{h^2}{2k_BT}(\frac{nr_H}{4\pi F_{1/2}(\eta)})^{\frac{2}{3}} \quad (8)$$

$$r_H = \frac{F_{1/2}(\eta)-F_{-1/2}(\eta)}{4F_0(\eta)^2}, \quad (9)$$

where h is Plank's constant, and r_H is the Hall coefficient.

Supplementary Note 6:

The fit of bipolar thermal conductivity for HT-NR

The electronic thermal conductivity can be divided into the contribution of single-type carriers and a bipolar term [11]

$$\kappa_{e-total} = \kappa_e + \kappa_b. \tag{10}$$

According to the Wiedemann-Franz law, the Lorenz number L can be expressed as [12]

$$L = \frac{\kappa_e + \kappa_b}{\sigma T}. \tag{11}$$

The term κ_e is the contribution of n-type carriers to thermal conductivity, which can be calculated using the SPB model, the details of which are shown in **Supplementary Note 5**.

The bipolar term κ_b can be calculated through the following formula [12]

$$\kappa_b = \frac{\sigma_n \sigma_p}{(\sigma_n + \sigma_p)^2} \left(\frac{E_g}{kT} + 4\right)^2 (\frac{k}{e})^2 \sigma T, \tag{12}$$

where E_g is the band gap at a certain temperature, k is the Boltzmann constant, σ is relevant electrical conductivity.

The HT-NR's bipolar diffusion thermal conductivity is observed in the intrinsic excitation region. At this time, majority carriers and minority carriers are nearly equal, so the above equation (**Eq. 12**) can be reduced as

$$\kappa_b = \frac{b}{(b+1)^2} \left(\frac{E_g}{kT} + 4\right)^2 (\frac{k}{e})^2 \sigma T, \tag{13}$$

in which the b is a ratio of mobilities for majority carrier (electrons) and minority carrier (holes). The value of E_g is obtained as follows.

The intrinsic carrier concentration depends exponentially on $-\frac{E_g}{2kT}$, as expressed in the following equation [7]

$$\ln n = -\frac{E_g}{2k} \frac{1}{T}. \tag{14}$$

The intrinsic energy gap E_g fitted from $ln(n)$-T^{-1} plot (**Figure S16a**) is 1.041 ± 0.078 eV for HT-NR. Thus, we fit the κ_b of HT-NR through **Eq. (13)** so that it satisfies $\kappa_{total} = \kappa_e + \kappa_L + \kappa_b$ (**Figure S16b**).

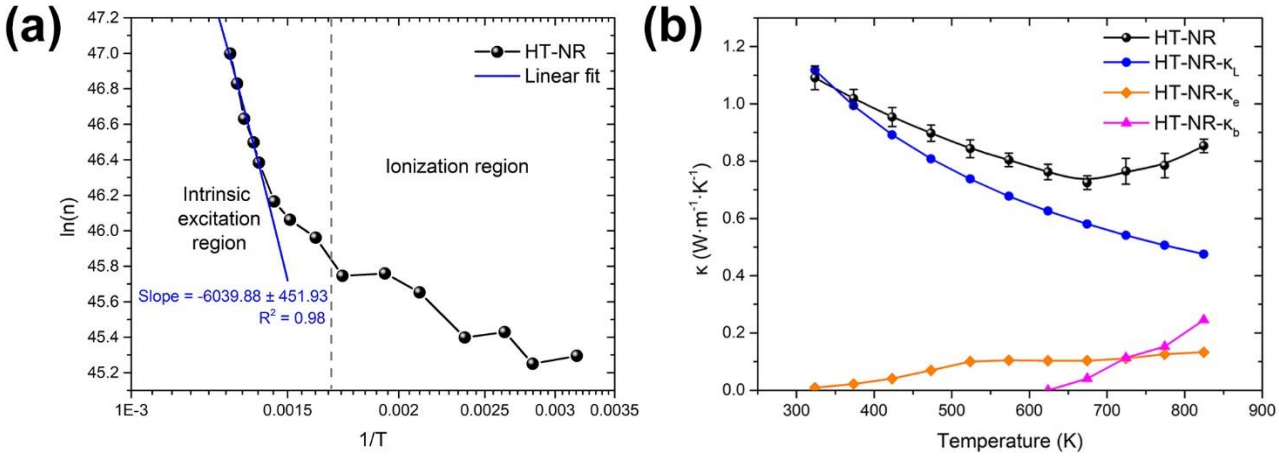

Figure S16. (a) *ln(n)-T*$^{-1}$ plot with its linear fit curve in intrinsic excitation region (723-773 K); (b) the simulated data (κ_e, κ_b and κ_L) from HT-NR's thermal conductivity.

Supplementary Note 7:

First-principles calculation details

The crystal structure of Bi_2S_3 was obtained from the Crystallography Open Database [13] (No. 1521540) with Pnma (62) space group, and its cell parameters are 11.170 Å, 11.319 Å, and 3.992 Å, respectively. The calculations of density of states (DOS) and band structure of Bi_2S_3 system were implemented in projected augmented plane-wave (PAW) method [14] via Vienna ab initio simulation package (VASP) [15]. The generalized gradient approximation (GGA) exchange and correlation function proposed by Perdew, Burke, and Ernzerhof (PBE) [16] is used to calculate the electronic structure. All the results were based on a 1×1×3 supercell with a 400-eV energy cutoff. Sampling was performed in the reciprocal space using the Monkhorst-Pack method [17] with 6×6×6 grids of k-points for the DOS calculations. The calculation path of high symmetry points in the first Brillouin zone of band structure is Γ–X–S–Y–Γ–Z–U–R–T. The energy convergence precision of the whole calculation process is below 10^{-6} eV/atom, while the Hellman-Feynman force is smaller than 0.01Å/atom in the optimized supercell. Since bismuth is a heavy element, the spin-orbit coupling (SOC) effect is considered in all DOS and band structure calculations to account for relativistic effects. DOS and band structure data were extracted via VASPKIT code [18].

The formation energy (E_f) of chlorine doping into different sites is calculated from the following equation [19],

$$E_f[Bi_2S_{3-x}Cl_y] = E_{tot}[Bi_2S_{3-x}Cl_y] - E_{tot}[Bi_2S_3, bulk] - \Sigma_i n_i \cdot \mu_i + q \cdot \varepsilon_f . \quad (15)$$

Where the $E_{tot}[Bi_2S_{3-x}Cl_y]$ is the total energy of Cl-doping system, $E_{tot}[Bi_2S_3, bulk]$ is the total energy of pristine Bi_2S_3 supercell, species i goes over Cl and S, n_i is the number of Cl atoms (positive) or S atoms (negative), μ_i is the chemical potential of species i, q is the charge states of defects, and ε_f is the Fermi level.

The phonon dispersion is calculated by using the Phonopy package [20] with VASP [21, 22]. The exchange-correlation energy functional is approximated by using local-density approximations (LDA). The plane-wave energy cutoff is set as 750 eV for both unit cell and supercell calculations, similar to Ref.[23]. The unit cell (20 atoms) is relaxed until the force is smaller than 10^{-5} eV/Å with an energy convergence threshold of 10^{-9} eV/Å and k-mesh of 4×4×12. A 2×2×3 supercell with k-mesh of 2×2×4 is used to calculate the forces of atoms with finite displacements, in order to calculate

the second order force constants. The Four-phonon extension [24] to the ShengBTE package [25] is used to calculate the three-phonon and four-phonon scattering phase spaces with phonon q-mesh of 4×4×8 and scalebroad factor of 0.005.

Supplementary Note 8:

BTE modeling of lattice thermal conductivity

To gain insight into the thermal transport and understand the relative importance of three-phonon (3ph) scattering, four-phonon (4ph) scattering, and extrinsic properties: defect, porosity, grain boundary, and impurities scattering in HT-NN and HT-NR materials, we fit the experimental data based on BTE [26-28]:

$$\kappa = \frac{1}{3N_q V_{cell}} \sum_{\lambda}^{3N_q} c_\lambda v_\lambda^2 \tau_\lambda \tag{16}$$

Here, N_q is the total number of $\mathbf{q}$ points sampled in the reciprocal space, V_{cell} is the volume of unit cell, $\lambda \equiv (\mathbf{q}, j)$ stands for a phonon mode with wavevector $\mathbf{q}$ and dispersion branch j, c_λ is the specific heat of phonon mode λ, v_λ is the phonon group velocity, and τ_λ is the phonon relaxation time. $c_\lambda = \frac{\hbar^2\omega^2}{k_B T^2} \frac{\exp(\frac{\hbar\omega}{k_B T})}{\left(\exp\left(\frac{\hbar\omega}{k_B T}\right)-1\right)^2}$. k_B is the Boltzmann constant, $\hbar$ is the reduced Planck's constant, T is the temperature, and ω is the angular frequency. In this work, a 6×6×18 $\mathbf{q}$ mesh is sampled. With the 60 phonon branches, there are 6×6×18×60 = 38,880 phonon modes that are included in the calculation of thermal conductivity.

The combined relaxation time incorporates the effects of 3ph scattering [29-32], 4ph scattering [33], crystal defect scattering [28, 30, 32, 34], nanopores [35, 36], grain boundary [29, 32, 36] and impurities [29, 31, 32, 34, 37] as:

$${\tau_p}^{-1} = {\tau_{3p}}^{-1} + {\tau_{4p}}^{-1} + {\tau_{def}}^{-1} + {\tau_{por}}^{-1} + {\tau_{gb}}^{-1} + {\tau_{imp}}^{-1} \tag{17}$$

Here,

$${\tau_{3p}}^{-1} = a\omega^2 T \exp\left(-\frac{\theta}{3T}\right) \approx a\omega^2 T \ \ (\text{when } T \gg \theta) \tag{18}$$

$${\tau_{4p}}^{-1} = b\omega^4 T^2 \tag{19}$$

$${\tau_{def}}^{-1} = c\omega^4 \tag{20}$$

$$\tau_{por}{}^{-1} = \frac{P}{2}\tau_{bulk}{}^{-1} + \frac{3P}{2}\frac{v}{D_{pore}} = \frac{P}{2}(a\omega^2 T + b\omega^4 T^2) + \frac{3P}{2}\frac{v}{D_{pore}} \tag{21}$$

$$\tau_{gb}{}^{-1} = \frac{v}{D_{grain}} \tag{22}$$

$$\tau_{imp}{}^{-1} = \frac{\pi}{2}\omega^2 \sum_i g_i D_i(\omega) \tag{23}$$

Here, a, b and c are experimental fitting parameters corresponding to 3ph scattering, 4ph scattering, and defect scattering. P is the porosity, D_{pore} is the average size of the nanopores, D_{grain} is the average grain size, respectively. Similarly, $g_i = f_i\left(\frac{\Delta M_i}{M_i}\right)^2$, where f_i is the number concentration of impurity at the host species i, and ΔM_i is the mass difference between impurity and host atoms, M_i is the mass of host species i. $D_i(\omega)$ is the normalized phonon partial density of states of the host species. The normalization should satisfy $\sum_i \int D_i(\omega)\mathrm{d}\omega = 1$.

Since 3ph and 4ph scatterings are intrinsic mechanisms in Bi_2S_3, their fitting parameters a and b are common for both samples: HT-NN and HT-NR. The two samples have different extrinsic properties; thus, they have different extrinsic parameters corresponding to porosity, pore size, grain size, and concentration of impurities. The fitting parameters for crystal defects are c_1 and c_2 for samples HT-NN and HT-NR, respectively.

In the fitting process, there are four fitting parameters: a, b, c_1 and c_2. Totally 17 experimental data, including all 11 data of HT-NN and the first 6 data (those at T < 600 K) of HT-NR, are used in the fitting process. The fitted curves agree well with all 17 data. The remaining data (those at T > 600 K) for HT-NR contains bipolar thermal conductivity contribution and therefore are not used in the lattice thermal conductivity fitting process.

Supplementary Note 9:

Determining the dominant scattering mechanism by a dimensionless parameter α_{BD} when μ increases exponentially with temperature.

The α_{BD} is a ratio of effective Bohr radius (α_B^*) and Debye screening length (L_D), which can be used to describe the screening capability of the material [38]

$$\alpha_{BD} = \frac{a_B^*}{L_D} = \frac{4\pi\hbar^2}{m_b^* e}\sqrt{\frac{n\varepsilon_r\varepsilon_0}{N_v kT}}, \tag{24}$$

in which, $\hbar$ is the reduced Plank's constant, m_b^* is effective mass for conduction band, n is carrier concentration, ε_r is the relative dielectric constant, ε_0 is the vacuum permittivity, N_v is the valley degeneracy, k is the Boltzmann constant. If α_{BD} is greater than 1, the region where electrons can move freely is much larger than the that affected by impurity ions, and the screening effect of impurity ions is enhanced, so the ionization impurity scattering can be ignored. On the contrary, if α_{BD} is a small value, ionization impurity scattering is the dominant mechanism.

The required parameters and the result are listed in **Table S4** below.

Table S4. The relative parameters to estimate α_{BD} for Cl-doped Bi_2S_3. The vacuum permittivity of 10.9 is from the reference [39].

m_b^* (from DFT)	N_v (from DFT)	ε_r (from reference)	n (from Hall)	α_{BD}
0.357 m_e	2	10.9	4×10^{25} m^{-3}	1.74

The value of α_{BD} for Bi_2S_3 is > 1, which indicates that the influence of ionized impurities on carrier transport is negligible. The dominant mechanism is grain boundary scattering.

Supplementary Note 10

The energy gap of Bi_2S_3 in high temperatures.

The intrinsic carrier concentration depends exponentially on $-\frac{E_g}{2kT}$, as depicted in the following equation [Kittel, Charles, and Paul McEuen. *Kittel's Introduction to Solid State Physics*. John Wiley & Sons, 2018.]

$$\ln n = -\frac{E_g}{2k}\frac{1}{T}, \quad \textbf{(25)}$$

in which k is the Boltzmann constant. The E_g values fitted from $ln(n)$-T^{-1} plot above 723 K are 1.041 ± 0.078 eV for HT-NR and 1.173 ± 0.005 eV for HT-NN, respectively.

Both band gaps in high-temperature region are slightly smaller than those measured at room temperature in literature (1.3-1.7 eV) [40-42]. We speculate that the thermal motion of the atoms increases at high temperature, resulting in larger atomic distances and larger lattice constants. This small increase in lattice constant weakens the periodic potential field of the system but has little effect on the overlap of electron clouds, thus the band gap is narrowed [11, 43].

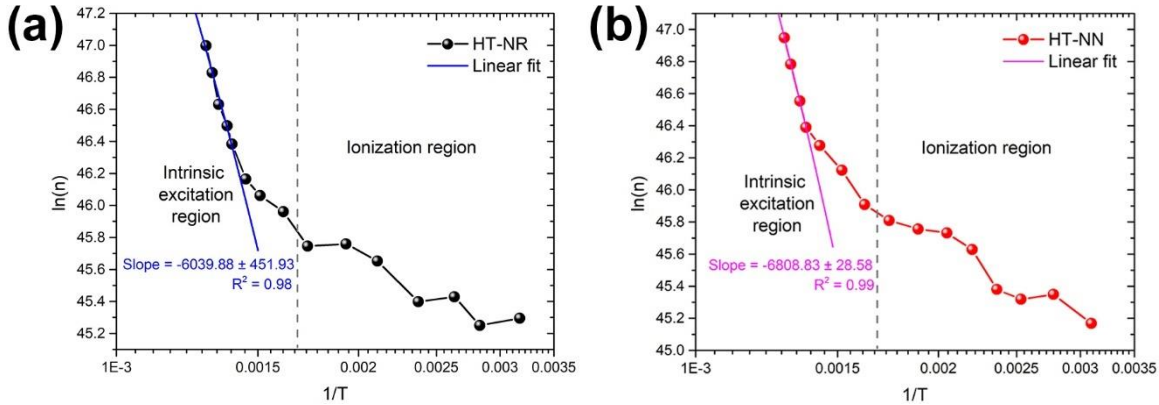

Figure S17. $ln(n)$-T^{-1} plot with its linear fit curve in intrinsic excitation region (723-773 K).

Supplemental References

[1] J.Y.W. Seto, The electrical properties of polycrystalline silicon films, J. Appl. Phys. 46 (1975), 5247-5254.

[2] T.J. Slade, J.A. Grovogui, J.J. Kuo, S. Anand, T.P. Bailey, M. Wood, C. Uher, G.J. Snyder, V.P. Dravid, M.G. Kanatzidis, Understanding the thermally activated charge transport in $NaPb_mSbQ_{m+2}$ (Q = S, Se, Te) thermoelectrics: weak dielectric screening leads to grain boundary dominated charge carrier scattering, Energy & Environmental Science 13 (2020), 1509-1518.

[3] J. Martin, L. Wang, L. Chen, G.S. Nolas, Enhanced Seebeck coefficient through energy-barrier scattering in PbTe nanocomposites, Phys. Rev. B 79 (2009), 115311.

[4] T.R. Wei, C.F. Wu, X. Zhang, Q. Tan, L. Sun, Y. Pan, J.F. Li, Thermoelectric transport properties of pristine and Na-doped $SnSe_{1-x}Te_x$ polycrystals, Phys. Chem. Chem. Phys. 17 (2015), 30102-30109.

[5] F.K. Lotgering, Topotactical reactions with ferrimagnetic oxides having hexagonal crystal structures—I, Journal of Inorganic and Nuclear Chemistry 9 (1959), 113-123.

[6] T.M. Tritt, Thermal conductivity: theory, properties, and applications. Springer Science & Business Media: 2005.

[7] C. Kittel, P. McEuen, *Kittel's Introduction to Solid State Physics*. John Wiley & Sons: 2018.

[8] D. Chakraborty, L. de Sousa Oliveira, N. Neophytou, Enhanced Phonon Boundary Scattering at High Temperatures in Hierarchically Disordered Nanostructures, J. Electron. Mater. 48 (2019), 1909-1916.

[9] S. Foster, N. Neophytou, Effectiveness of nanoinclusions for reducing bipolar effects in thermoelectric materials, Computational Materials Science 164 (2019), 91-98.

[10] Ultrahigh power factor and thermoelectric performance in hole-doped single-crystal SnSe, Science 351 (2016), 141-144.

[11] C.J. Glassbrenner, G.A. Slack, Thermal Conductivity of Silicon and Germanium from 3°K to the Melting Point, Phys. Rev. 134 (1964), A1058-A1069.

[12] J.R. Drabble and H.J. Goldsmid, Thermal conduction in semiconductors, Vol. 4., Pergamon Press, Oxford, 1961. https://doi.org/10.1002/bbpc.19620660617

[13] S. Gražulis, A. Daškevič, A. Merkys, D. Chateigner, L. Lutterotti, M. Quirós, N.R. Serebryanaya, P. Moeck, R.T. Downs, A. Le Bail, Crystallography Open Database (COD): an open-access collection of crystal structures and platform for world-wide collaboration, Nucleic Acids Res. 40 (2012), D420-D427.

[14] P.E. Blöchl, Projector augmented-wave method, Phys. Rev. B 50 (1994), 17953-17979.

[15] G. Kresse, J. Furthmüller, Efficient iterative schemes for ab initio total-energy calculations using a plane-wave basis set, Phys. Rev. B 54 (1996), 11169-11186.

[16] J.P. Perdew, K. Burke, M. Ernzerhof, Generalized Gradient Approximation Made Simple, Phys. Rev. Lett. 77 (1996), 3865-3868.

[17] H.J. Monkhorst, J.D. Pack, Special points for Brillouin-zone integrations, Phys. Rev. B 13 (1976), 5188-5192.

[18] V. Wang, N. Xu, J. Liu, G. Tang, W. Geng, VASPKIT: A user-friendly interface facilitating high-throughput computing and analysis using VASP code, Comput. Phys. Commun. 267 (2021), 108033.

[19] C. Freysoldt, B. Grabowski, T. Hickel, J. Neugebauer, G. Kresse, A. Janotti, C.G. Van de Walle, First-principles calculations for point defects in solids, Rev. Mod. Phys. 86 (2014), 253-305.

[20] A. Togo, I. Tanaka, First principles phonon calculations in materials science, Scripta Mater. 108 (2015), 1-5.

[21] G. Kresse, J. Hafner, Ab initio molecular dynamics for liquid metals, Phys. Rev. B 47 (1993), 558-561.

[22] G. Kresse, J. Hafner, Ab initio molecular-dynamics simulation of the liquid-metal--amorphous-semiconductor transition in germanium, Phys. Rev. B 49 (1994), 14251-14269.

[23] Y. Zhao, K.T.E. Chua, C.K. Gan, J. Zhang, B. Peng, Z. Peng, Q. Xiong, Phonons in Bi_2S_3 nanostructures: Raman scattering and first-principles studies, Phys. Rev. B 84 (2011), 205330.

[24] Z. Han, X. Yang, W. Li, T. Feng, X. Ruan, FourPhonon: An extension module to ShengBTE for computing four-phonon scattering rates and thermal conductivity, Comput. Phys. Commun. 270 (2022), 108179.

[25] W. Li, J. Carrete, N. A. Katcho, N. Mingo, ShengBTE: A solver of the Boltzmann transport equation for phonons, Comput. Phys. Commun. 185 (2014), 1747-1758.

[26] R. Peierls, R.E. Peierls, Quantum theory of solids. Oxford University Press, 1955.

[27] P.G. Klemens, Thermal Conductivity and Lattice Vibrational Modes, In *Solid state physics* (Vol. 7, pp. 1-98), Academic Press, 1958. https://doi.org/10.1016/S0081-1947(08)60551-2

[28] T. Feng, X. Ruan, Prediction of Spectral Phonon Mean Free Path and Thermal Conductivity with Applications to Thermoelectrics and Thermal Management: A Review, Journal of Nanomaterials 2014 (2014), 206370.

[29] J. Fang, Y. Huang, C.M. Lew, Y. Yan, L. Pilon, Temperature dependent thermal conductivity of pure silica MEL and MFI zeolite thin films, J. Appl. Phys. 111 (2012), 054910.

[30] Y. Hudiono, A. Greenstein, C. Saha-Kuete, B. Olson, S. Graham, S. Nair, Effects of composition and phonon scattering mechanisms on thermal transport in MFI zeolite films, J. Appl. Phys. 102 (2007), 053523.

[31] B. Xu, T. Feng, M.T. Agne, L. Zhou, X. Ruan, G.J. Snyder, Y. Wu, Highly Porous Thermoelectric Nanocomposites with Low Thermal Conductivity and High Figure of Merit from Large-Scale Solution-Synthesized Bi2 Te2.5 Se0.5 Hollow Nanostructures, Angew. Chem. Int. Ed. Engl. 56 (2017), 3546-3551.

[32] G.P. Srivastava, *The physics of phonons*. Routledge: 2019. https://doi.org/10.1201/9780203736241

[33] T. Feng, L. Lindsay, X. Ruan, Four-phonon scattering significantly reduces intrinsic thermal conductivity of solids, Phys. Rev. B 96 (2017), 161201.

[34] T. Feng, B. Qiu, X. Ruan, Coupling between phonon-phonon and phonon-impurity scattering: A critical revisit of the spectral Matthiessen's rule, Phys. Rev. B 92 (2015), 235206.

[35] R. Dettori, C. Melis, X. Cartoixà, R. Rurali, L. Colombo, Model for thermal conductivity in nanoporous silicon from atomistic simulations, Phys. Rev. B 91 (2015), 054305.

[36] B. Xu, T. Feng, Z. Li, S.T. Pantelides, Y. Wu, Constructing Highly Porous Thermoelectric Monoliths with High-Performance and Improved Portability from Solution-Synthesized Shape-Controlled Nanocrystals, Nano Lett. 18 (2018), 4034-4039.

[37] S.-i. Tamura, Isotope scattering of dispersive phonons in Ge, Phys. Rev. B 27 (1983), 858-866.

[38] C. Hu, K. Xia, C. Fu, X. Zhao, T. Zhu, Carrier grain boundary scattering in thermoelectric materials, Energy Environ. Sci. 15 (2022) 1406-1422

[39] A. Cantarero, J.P. Martínez, A. Seguba, A. Chevy, Refractive index of bismuth sulfide in the infrared region, Physica Status Solidi (a) 101 (1987), 603-609.

[40] P. Larson, V.A. Greanya, W.C. Tonjes, R. Liu, S.D. Mahanti, C.G. Olson, Electronic structure of Bi_2X_3 (X=S,Se,T) compounds: Comparison of theoretical calculations with photoemission studies, Phys. Rev. B 65 (2002), 085108.

[41] J. Ni, Y. Zhao, T. Liu, H. Zheng, L. Gao, C. Yan, L. Li, Strongly Coupled Bi_2S_3@CNT Hybrids for Robust Lithium Storage, Adv. Energy Mater. 4 (2014), 1400798.

[42] M. Bernechea, Y. Cao, G. Konstantatos, Size and bandgap tunability in Bi_2S_3 colloidal nanocrystals and its effect in solution processed solar cells, Journal of Materials Chemistry A 3 (2015), 20642-20648.

[43] S. Namjoo, A.S.H. Rozatian, I. Jabbari, Influence of lattice expansion on the topological band order of $InAs_xSb_{1-x}$ (x=0, 0.25, 0.5, 0.75, 1) alloys, J. Alloy. Compd. 628 (2015), 458-463.